Author-Accepted Manuscript (Post-Review Version)

Dynamics, interactions and delays of the 2019 Ridgecrest rupture sequence

Taufiq Taufiqurrahman, Alice-Agnes Gabriel, Duo Li, Thomas Ulrich, Bo Li,
Sara Carena, Alessandro Verdecchia, and František Gallovič

The final version of this work was published in *Nature* and is available at:

https://doi.org/10.1038/s41586-023-05985-x

Title: Dynamics, interactions and delays of the 2019 Ridgecrest rupture sequence

Authors: Taufiq Taufiqurrahman[1], Alice-Agnes Gabriel[2,1*], Duo Li[1], Thomas Ulrich[1], Bo Li[1], Sara Carena[1], Alessandro Verdecchia[3,4], Frantisek Gallovic[5]

Affiliations: [1] Department of Earth and Environmental Sciences, Ludwig-Maximilians-Universität München, Munich, Germany
[2] Institute of Geophysics and Planetary Physics, Scripps Institution of Oceanography, University of California San Diego, La Jolla, USA
[3] Department of Earth and Planetary Sciences, McGill University, Montreal, Quebec, Canada
[4] Institute of Geology, Mineralogy and Geophysics, Ruhr-University Bochum, Bochum, Germany
[5] Department of Geophysics, Faculty of Mathematics and Physics, Charles University, Prague, Czech Republic

*Corresponding author; E-mail:
Alice-Agnes Gabriel, algabriel@ucsd.edu

Summary

The observational difficulties and the complexity of earthquake physics have rendered seismic hazard assessment largely empirical. Despite increasingly high-quality geodetic, seismic, and field observations, data-driven earthquake imaging yields stark differences and physics-based models explaining all observed dynamic complexities are elusive. Here we present data-assimilated 3D dynamic rupture models of California's biggest earthquakes in more than 20 years: the moment magnitude (M_{w}) 6.4 Searles Valley and M_{w}7.1 Ridgecrest sequence breaking multiple segments of a non-vertical quasi-orthogonal conjugate fault system (*1*). Our models use supercomputing to find the link between the two earthquakes. We explain strong-motion, teleseismic, field mapping, high-rate GPS, and space geodetic datasets with earthquake physics. We find that regional structure, ambient long- and short-term stress, and dynamic and static fault system interactions driven by overpressurized fluids and low dynamic friction, are conjointly crucial to understand the dynamics and delays of the sequence. We demonstrate that joint physics-based and data-driven illumination of the mechanics of complex fault systems and earthquake sequences is possible when reconciling dense earthquake recordings, 3D regional structure and stress models. We foresee that physics-based interpretation of big observational datasets will have a transformative impact on future geohazard mitigation.

Main Text:

The July 4 and 5, 2019, M_{w}6.4 Searles Valley foreshock and M_{w}7.1 Ridgecrest mainshock, California, are prominent examples of large, well-recorded earthquakes (*1–3*) that provide unique opportunity to advance our understanding of the mechanics and regional hazard of active multi-fault systems. The sequence cascaded across hierarchically-interlaced antithetic faults (*4*), part of the presumably immature Eastern California Shear Zone (ECSZ). The ECSZ accommodates

an increasing fraction of regional tectonic forces (*5*) while developing into a major tectonic boundary. Multi-scale block rotation in its transtensional deformation regime leads to ubiquitous conjugate and subparallel strike-slip faulting, which may promote the initiation and segmentation of large earthquakes, which can occur simultaneously or in quick succession (*6, 7*).

Both earthquakes were highly complex (*8*), including likely fault reactivation (*9, 10*). Peculiarly, the largest events were set apart in time by 34 hr (*11, 12*) while driving aftershocks, shallow aseismic creep, and swarm activity (*13, 14*). Numerous inversion-based earthquake models (e.g., (*15*)) use this exceptionally high-quality dataset, but, despite the good coverage of geodetic and seismic observations, the proposed slip models and their interpretations differ starkly. It is still a matter of debate which fault segments actively slipped, and which regional conditions promote the general occurrence of conjugate earthquake cascades. Data-driven approaches are inherently limited in their ability to uniquely resolve fault interactions and are specifically challenged by multiple slip-episodes occurring close in time and activating partially overlapping fault segments, all common characteristics of earthquake sequences in multi-fault systems. Thus, a unifying approach, capable to jointly explain independent data-sets and intriguing dynamic features, such as the delayed triggering of the mainshock, is required, but remains elusive.

We present the first tightly data-constrained and physics-based approach that disentangles the competing and non-unique views (*15*) of the Ridgecrest foreshock and mainshock and their interrelationship, with general implications for the often underestimated hazard posed by multi-fault earthquakes. We address the fundamental questions about the sequence in a data-fused yet physics-based manner, such as: What governs the initiation, propagation and arrest of coseismic slip on immature, geometrically complex faults? How do earthquake sequences dynamically interact across multi-fault systems? What is the role of heterogeneity in the subsurface and in the ambient stress field, including heterogeneity from historical and recent events, for the

dynamics of large earthquakes?

Our supercomputing-empowered 3D linked foreshock-mainshock dynamic rupture models (see Methods) provide insight into the multi-stage dynamics of how an immature conjugate fault system yields and slides. We reveal foreshock and mainshock dynamics that are characterized by simultaneous rupture of conjugate faults, mixed crack- and pulse-like propagation and strongly interact interseismically. By combining multi-disciplinary and multi-scale observations, we constrain the mechanical properties of the fault system to be statically strong but dynamically weak. Dynamic rupture of a statically-strong yet dynamically-weak fault system is driven by overpressurized fluids and low dynamic friction in our models. This concept, first proposed to reconcile the San Andreas heat flow paradox (*16*), allows faults to operate at low average prestress while facilitating multi-fault cascading rupture dynamics (*17*). While dynamic fault weakening may not operate during all natural earthquakes and other mechanisms such as frictional heterogeneity may explain multi-fault ruptures, we show that the interplay of 3D fault stress, strength and geometries remains important even if all faults are dynamically weak.

We demonstrate how a novel 3D stress model fusing regional tectonics and co- and postseismic stress changes of historical earthquakes drives and delays an earthquake sequence through space and time. Our multi-fault model is the first to unify dense strong-motion and teleseismic, field mapping, high-rate GNSS, and space geodetic foreshock and mainshock datasets with earthquake physics. For comparison in the near- and far-field, we also present a new frequency-dependent aftershock-calibrated back-projection analysis ((*18*), see Methods) and kinematic parametric source inversion ((*19*), see Methods) using strong-motion data, accounting for the geometric fault complexity that we find is required in dynamic modeling.

From tectonics to dynamic rupture

We apply novel assimilation methods fusing tectonic, structural, coseismic, and interseismic data to jointly inform physics-based dynamic rupture simulations. First, integrating InSAR, satellite imagery, relocated seismicity, and selected focal mechanisms, we construct ((*20*), see Methods) a non-vertical, quasi-orthogonal cross-cutting 3D fault system (Fig. 1). It consists of four geometrically complex fault segments (Fig. S1), all of which slip coseismically during either the foreshock or mainshock or both: three NW-SE trending right-lateral faults, F1, F3, and F4, and a conjugate NE-SW trending left-lateral fault, F2. The largest fault, F3, is helically shaped, consistent with the geometry of deep ductile shear localization (*21*). We next embed this fault system in a 3D Earth structure combining a 3D community velocity model ((*22*), see Methods) and a 2D community stress model (*23*) representing the regional state of stress in the southern California upper crust (Figs. 1a, S2). To account for fault-local stress heterogeneity due to past seismicity, we incorporate a new 3D model of the cumulative co- and postseismic stress changes of major historical and recent earthquakes spanning the last $\sim$1400 years, extended in the course of this study from (*24*) (Fig. 1b). We combine the resulting heterogeneous ambient stress model with linear depth-dependence of the effective vertical stress (see Methods).

There is little consensus about the effective strength of active faults (*25*). We demonstrate that a large frictional strength drop, requiring statically strong but dynamically weak faults (Table S2), promotes dynamic cascading of rupture across the Ridgecrest system of vastly varying fault orientations.We use a laboratory-based modern friction law (see Methods) that features dramatically rate-dependent dynamic weakening (*26*), while being compatible with the high static frictional strength of rocks and multi-fault cascading rupture dynamics (*17*). We introduce depth-dependent frictional parameters to account for shallow (above 1.8 km depth)

velocity-strengthening, and along-fault variations in seismogenic depth, as inferred from aftershock locations (*1*), decreasing from a maximum of $\sim$11 km near the foreshock hypocenter toward north and south (Fig. S3). Overpressurized fault zone fluids, above the hydrostatic pressure gradient, reduce the apparent strength of faults by decreasing the effective normal stress. Our model suggests that the Ridgecrest fault system is embedded in a region of elevated pore fluid pressure, with fluid pressure higher on the foreshock faults than on the mainshock ones (Fig. S4).

In dynamic rupture models, the ratio of potential stress drop to frictional breakdown strength (R) is a key parameter controlling earthquake kinematics, dynamic triggering ("cascading") potential, and dynamic slip tendency (see Methods). We prescribe the prestress relatively to strength drop on a virtual, optimally-oriented fault within the model domain as $R_0 = 0.8$. This introduces spatially-variable relative fault prestress $R \leq R_0$ (Fig. 1c), and brings more optimally-oriented fault segments locally close to being critically prestressed. The orientation of all regional principal stress components, the relative magnitude of the intermediate principal stress, the choice of R_0, and the cumulative co- and postseismic stress changes (Fig. 1d) together define the complex 3D pre-sequence stress state that governs the dynamics of the sequence. The conjugate fault F2 and central portions of F3 are well oriented, as illustrated by R locally approaching $R_0 = 0.8$, and simultaneously close to critically prestressed, as the ratio of shear to effective normal prestresses is high (Fig. S5). In contrast, F1, F4, and the southern and northern parts of F3 show considerably lower R and are therefore farther from critical prestress, reflecting geometrical deviation from optimal orientation with respect to the complex 3D stress model.

We use data-inferred key characteristics of both earthquakes, specifically hypocenter and aftershock locations (*1, 27*), moment release rate (*8, 28, 29*) and the delay between foreshock and mainshock, to find the required dynamic parameters R_0, pore fluid pressure and rupture

initiation overstress using several systematic dynamic rupture simulations (see Methods). We do not invert space geodesy, strong-motion, high-rate GPS, or teleseismic recordings, but use them for retrospective validation of our earthquake source models. While the need for *ad hoc* rupture nucleation at prescribed hypocenters is a limitation of dynamic rupture simulations (see Methods), analyzing the minimum perturbation leading to self-sustained foreshock and mainshock earthquake dynamics matching observations provides insights into the underlying physics of the cascading rupture sequence. We find that our observationally-constrained model balances the dynamic viability of sustained foreshock and mainshock dynamic rupture scenarios with realistic stress drop, rupture speed, and fault slip.

Foreshock cross-fault earthquake dynamics

Our earthquake model of the M_{w}6.4 Searles Valley foreshock features highly complex dynamics across conjugate faults while failing to coseismically trigger the mainshock. Joint seismological and geodetic (*30*), and conceptual dynamic (*31, 32*) models imply a cross-fault rupture path, initiating as deep slip on a right-lateral fault segment (F1, Fig. 2a) and continuing on an almost orthogonally interlocked left-lateral segment (F2). Whereas F2 surface rupture was traced, satellite images (*33*) give no indication of surface rupture along F1.

Our spontaneous dynamic rupture simulations reproduce conjugate rupture observations, and find that foreshock-mainshock fault system interactions are important in facilitating the subsequent mainshock dynamics. Rupture initiates (see Methods) close to the F1-F2 fault intersection, which may be a general prerequisite for simultaneous rupture of conjugate faults as suggested from field observations (*6*). Early and deep right-lateral dynamic rupture across F1 activates the conjugate, critically prestressed left-lateral F2 leading to complex foreshock slip evolution (Fig. 2a and Video S1). At 2 s, rupture takes the form of a near-symmetric, circular crack propagating across both faults, but with higher slip rates (up to $\sim$3 m/s) on F1 (Fig. 2a). At

5 s, slip on F1 spontaneously ceases without reaching the surface due to this fault's non-optimal orientation and lower-than-critical prestress. In contrast, dynamic rupture on F2 continues to the SW and up-dip and breaks the surface, until terminated by pronounced stopping phases. Importantly, F2 rupture takes the form of a narrow slip pulse which re-accumulates a significant amount of shear stress across F2, aiding subsequent reactivation (*34*) during the mainshock.

The physics-based dynamic model agrees with data-driven kinematic models that assume comparable fault geometries. Fig. 2b showcases the overall agreement of the final slip distribution with a newly inferred kinematic parametric source inversion (PSI) of strong-motion data (see Methods). The dynamic rupture model yields depth-confined (8–11 km) right-lateral slip on F1, and widespread left-lateral slip on F2 including pronounced surface rupture (Fig. 2b). The maximum fault slip reaches $\sim$1.5 m on F1 near the hypocenter and $\sim$1 m on F2 near the surface. The dynamic rupture scenario generates moment magnitude M_{w} 6.5, in agreement with observations (*8, 28, 29*). Dynamic rupture speed is increasing from 1.5 km/s to 2.5 km/s with distance from the hypocenter, with an average fault-local speed of 2 km/s (Fig. S6). Whereas a direct comparison to observations is challenged by the medium size and multi-fault conjugate dynamics of the foreshock, the fault-local rupture speed agrees with the rupture velocity inferred in the PSI and other kinematic models (2.4-2.6 km/s) (*8*). Local differences of the PSI model include lower kinematic slip at depth on F1 and F2 and a more localized slip patch at shallow depth on F2. The latter is likely due to the Occam's razor principle implicitly preferring simple, localised slip distributions (see Methods).

Our new aftershock-calibrated back-projection (Table S3, see Methods) of Alaska array data implies orthogonal rupture during the foreshock (Fig. 2c), in agreement with our modeled earthquake dynamics. Back-projection captures $\sim$ 6 km NW propagating rupture on F1 followed by rupture to the SW tip of F2. From beam power analysis (Fig. 2d), the inferred high-frequency radiators on F1 and F2 appear equally significant. The normalized back-projection beam power

resembles the apparent array moment rate of the dynamic rupture model, specifically its two distinct peaks linked to consecutive slip on F1 and F2. In contrast, dominating slip on F2 is characteristic in other published kinematic models (Fig. 2d) and observational moment rates exhibit a weaker early phase than our dynamic model. This may reflect the generally lower sensitivity of kinematic methods to deep slip, especially when overprinted by dominating, shallow rupture. Contrarily, in our dynamic model, rupture along F1 is required to load and trigger rupture on F2.

The spontaneous dynamic rupture scenario reproduces key characteristics of space geodesy, strong-motion, high-rate GPS, and teleseismic recordings. The modeled fault-parallel offsets compare well with sub-pixel satellite image correlation measurements along the surface rupture of F2 (*33*) (Figs. 2e and S7a,b). Also, the modeled static surface deformation is in agreement with geodetic observations from GNSS and satellite imagery (Fig. 2f), and dominated by large, shallow slip on F2. We observe a striking match (Fig. 2g) between synthetic and observed near-fault 1 Hz continuous GPS data (*35*).The synthetics capture the shape and amplitude of characteristic waveform pulses well, such as the first EW strong pulse at CCCC and P595. Synthetic velocity time series agree with regional strong-motion data (Figs. 2h, S8) and long-period teleseismic recordings (Fig. S9a).

Dynamics of the Ridgecrest mainshock

We find that a realistic dynamic rupture scenario of the Ridgecrest mainshock needs to fully account for the stress changes due to the Searles Valley foreshock in addition to the regional complex 3D structure and ambient stress (Figs. S10, S11, and S12, see Methods). Modeling both events in the same dynamic rupture simulation, we find that the foreshock does not dynamically trigger the mainshock. The additional shear stress relative to our assumed fault strength and 3D prestress required to activate F3 at the mainshock hypocenter is 18 MPa peak

and $\sim$3 MPa averaged across the numerically determined minimal sized and smooth critical perturbation area (Fig. S13, see Methods). Locally higher fluid pressure reducing effective normal stress, a locally statically-weaker fault or combinations of heterogeneities may provide equivalent nucleation mechanisms at lower shear-stress increase.

Fig. 3a and Video S2 illustrate the modeled complex mainshock earthquake dynamics. During the first 5 s, a crack-like rupture expands bilaterally on F3, then smoothly terminates to the north due to locally lower prestress and less-optimal fault orientation (Fig. S5). The pronounced stress shadow of the M_{w} 6.4 foreshock (Fig. 4) leads to near-complete termination of southward rupture in the vicinity of the conjugate F2-F3 intersection, except for decelerated slip at greater depth (at 6.5 s, Fig. 3a). This deep, persistent and "tunneling" rupture pulse slowly regrows towards SE until the NW segment of F3 is entirely ruptured at 8.5 s. The conjugate segment F2 is re-activated while the main rupture front passes, aided by dynamic frictional restrengthening during the foreshock pulse-like rupture. Shallow parts of F4 are dynamically unclamped and slip during rupture of F3. Spontaneous dynamic rupture accumulates a continuous slip patch spanning F3 (Fig. 3b), modulated by the combined effects of fault geometry, ambient stress and structural heterogeneities, and foreshock stress shadows. Similarly to the foreshock, the modeled mainshock slip distribution agrees with kinematic models which assume comparable fault geometries within the range of inherent uncertainties, such as our strong-motion PSI model (Fig. 3b). Conjugate fault reactivation is suggested by our PSI, in our low frequency (0.1-0.5 Hz and 0.25-1 Hz) back-projection results (Fig. 3c and S14), as well as from joint inversion of InSAR, optical imagery, and GPS measurements (*10*).

Rupture speed is increasing by $\sim$25% from NW to SE and is strongly depth-dependent. The average apparent rupture speed is 2.5 km/s (Fig. S6) agreeing with our PSI model (2.1-2.4 km/s) and back-projection (2.5 km/s) (Fig. S14d). The moment release rate of our dynamic model, beam power evolution in our back-projection and other kinematic models including PSI

(Fig. 3d) consistently feature two peaks, which resemble the dynamic delay of F3 rupture when crossing the conjugate intersection with F2 in our model. Our modelled shallow rupture is slower and appears to agree better with data-driven estimates (*1, 8, 28, 30*), which may be due to less well constrained deeper fault zone geometry and structure.

Our synthetic F3-parallel surface offsets (Fig. 3e) reflect the along-strike dynamic rupture variability and peak close to the epicenter, in overall agreement with satellite images (*33*). The physics-based model matches coseismic geodetic observations, such as the orientation of the observed GPS displacements (Fig. 3f), surprisingly well. While forward modeling overshoots some static GPS amplitudes the modeled fault-parallel surface displacements are comparable with satellite imagery (Fig. S7c, d). The dynamic model reproduces key characteristics of continuous GPS (Fig. 3g), strong-motion (Figs. 3h, S15) and teleseismic waveforms (Fig. S9b). Pulse-like ground motion, with possibly increased damaging potential, was identified in near-fault observations of both earthquakes (*36*). We dynamically reproduce such strong impulsive signals at stations CLC, the closest station to the mainshock epicenter, MPM, WVP2, WMF, and WCS2 in the NW extension of rupture on F3, and CCC, close to the SE tip of rupture on F4 (Fig. 3h) due to a combination of partially pulse-like rupture, fault reactivation, strong directivity and fling effects due to the large lateral off-sets.

Conversations between earthquakes

The average dynamic on-fault stress drop is 4 MPa and 5.4 MPa during spontaneous foreshock and mainshock rupture, respectively, and varies with depth and along-strike for all activated faults (Fig. S16). This 30% higher mainshock stress drop directly relates to our dynamic models requiring differences in static pore fluid-pressure: the mainshock faults F3 and F4 are governed by an equivalently 30% lower pore fluid-pressure than foreshock faults F1, F2 (Fig. S4c) to achieve realistic levels of fault slip, stress drop and dynamically viable rupture cascading for

both events in the same model.

Foreshock dynamic rupture induces an absolute shear stress perturbation of at most $\sim$0.8 MPa at the mainshock hypocenter (Fig. 4a). With peak normal stress changes of $\sim$0.2 MPa additionally clamping and unclamping F3 (inset of Fig. 4a), both perturbations are not sufficient to dynamically trigger the mainshock rupture. Whilst our model suggests that dynamic triggering of the mainshock is mechanically inconceivable, it also shows that the complex foreshock Coulomb stress changes bring the mainshock hypocentral area closer to failure: the mainshock hypocenter of F3 is located within a narrow band experiencing positive Coulomb stress change of up to +0.25 MPa (Fig. 4b, see Methods).

The modeled foreshock rupture spontaneously terminates on F1, without reaching the surface and in $\sim$3 km horizontal distance to the F3 mainshock hypocenter. This gap in dynamic slip agrees with the inferred gap in relocated aftershocks following the foreshock (*1*), which was successively filled by a series of moderate-sized earthquakes (*37*), including a M_{w}5.4 earthquake within 2 km of the mainshock hypocenter. The static Coulomb stress changes of this event, however, were found to be negative at the mainshock hypocenter (*11*), although not well constrained.

Our models do not include stress changes due to aseismic processes such as postseismic slip and deep fault creep. The shear stress carried by afterslip is potentially considerable, implying interaction of coseismic and postseismic slip and their stresses (*12*). We analytically estimate ((*38*), see Methods) a peak shear stress increase of 2.5-4.5 MPa for an average afterslip creep front speed of 3 km in 34 hr and our assumed effective normal stress of 20.5 MPa at 8 km hypocentral depth. Seamlessly modelling the full spectrum of slip will be important to capture the interactions between foreshocks, mainshocks and aftershocks (*39, 40*).

The distribution of surface rupture and damage mapped from field and aerial observations (*1, 41, 42*) (Figs. 5a, c) align with our prescribed fault geometries and the modeled dynamically-

induced off-fault yielding (see Methods), which accumulates in the vicinity of complexities in fault system geometry (Fig. 5b). The moment contribution of off-fault plastic strain (see Methods) in our models is non-negligible, accounting for 3% and 8%, respectively, of the total seismic moments of the modeled foreshock (M_{w}6.45) and mainshock (M_{w}=7.01). We observe a shallow slip deficit (SSD) of up to 20% above 2 km depth (Inset Fig. 5b), which agrees with joint GPS, ground-motion and InSAR inversion (*12*).

We showcase the sensitivity of our physics-based models in four alternative scenarios including: mainshock dynamic rupture models (i) not accounting for the foreshock stress changes (Fig. S10); (ii) in addition not incorporating the long-term ΔCFS (Fig. S11); and combined foreshock and mainshock models (iii) omitting the long-term ΔCFS (Figs. S12, S17); and (iv) loaded with an alternative community ambient stress model (Fig. S18). Local rupture dynamics as well as the dynamic activation of segments of the sequence change when key modeling ingredients are altered (Fig. S19, see Methods). Particularly, not incorporating the long-term ΔCFS prevents to correctly capture the conjugate, partially surface-breaking character of the foreshock rupture.

Using a rate-and-state friction law with strong velocity-weakening facilitates the concept of statically strong and dynamically weak faults. If we assumed higher dynamic strength, our relative prestress would decrease (Eq.(9), see Methods). The dynamic rupture cascading potential may then be restored by local stress, strength or pore fluid pressure changes reflecting natural fault zone heterogeneity. For example, concentrating relative prestress at depth would allow us to approximate the expected effects of deep aseismic creep (*17, 21*).

By assimilating models and data of structural characteristics, tectonic stress, seismogenic depth and long-term stress changes, we constrain multi-fault dynamic rupture scenarios that self-consistently intertwine the 2019 Searles Valley and Ridgecrest multi-fault earthquake dynamics, and unify seismic, geodetic, and geological observations. The match with observations,

achieved across scales, is remarkable, given we do not solve an inverse problem. Including small-scale heterogeneities may improve physics-based synthetics at higher frequencies (*43*). Our approach demonstrates that data-driven and physics-based modeling can be combined to shed light on the underlying physics of cascading multi-fault earthquake sequences. Our results imply that the long-term and short-term, as well as the dynamic and static fault system interaction is crucial for future seismic hazard assessment of active multi-fault systems.

References

1. Ross, Z. E. *et al.* Hierarchical interlocked orthogonal faulting in the 2019 Ridgecrest earthquake sequence. *Science* **366**, 346–351 (2019).

2. Hauksson, E., Jones, L. M., Hutton, K. & Eberhart-Phillips, D. The 1992 Landers earthquake sequence: Seismological observations. *J. Geophys. Res. Solid Earth* **98**, 19835–19858 (1993).

3. Hamling, I. J. *et al.* Complex multifault rupture during the 2016 Mw 7.8 Kaikoura earthquake, New Zealand. *Science* **356**, eaam7194 (2017).

4. DuRoss, C. B. *et al.* Surface displacement distributions for the July 2019 Ridgecrest, California, earthquake ruptures. *Bull. Seismol. Soc. Am.* **110**, 1400–1418 (2020).

5. Zeng, Y. & Shen, Z. A fault-based model for crustal deformation, fault slip rates, and off-fault strain rate in California. *Bull. Seismol. Soc. Am.* **106**, 766–784 (2016).

6. Fukuyama, E. Dynamic faulting on a conjugate fault system detected by near-fault tilt measurements. *Earth Planet Sp.* **67**, 38 (2015).

7. Kato, A., Sakai, S., Matsumoto, S. & Iio, Y. Conjugate faulting and structural complexity on the young fault system associated with the 2000 Tottori earthquake. *Commun. Earth. Environ.* **2**, 13 (2021).

8. Chen, K. *et al.* Cascading and pulse-like ruptures during the 2019 Ridgecrest earthquakes in the Eastern California Shear Zone. *Nat. Commun.* **11**, 22 (2020).

9. Shi, Q. & Wei, S. Highly heterogeneous pore fluid pressure enabled rupture of orthogonal faults during the 2019 Ridgecrest Mw7.0 earthquake. *Geophys. Res. Lett.* **47**, e2020GL089827 (2020).

10. Magen, Y., Ziv, A., Inbal, A., Baer, G. & Hollingsworth, J. Fault rerupture during the July 2019 Ridgecrest earthquake pair from joint slip inversion of InSAR, optical imagery, and GPS. *Bull. Seismol. Soc. Am.* **110**, 1627–1643 (2020).

11. Jin, Z. & Fialko, Y. Finite slip models of the 2019 Ridgecrest earthquake sequence constrained by space geodetic data and aftershock locations. *Bull. Seismol. Soc. Am.* **110**, 1660–1679 (2020).

12. Qiu, Q., Barbot, S., Wang, T. & Wei, S. Slip complementarity and triggering between the foreshock, mainshock, and afterslip of the 2019 Ridgecrest rupture sequence. *Bull. Seismol. Soc. Am.* **110**, 1701–1715 (2020).

13. Shelly, D. R. A high resolution seismic catalog for the initial 2019 Ridgecrest earthquake sequence: foreshocks, aftershocks, and faulting complexity. *Seismol. Res. Lett.* **91**, 1971–1978 (2020).

14. Cheng, Y. & Ben-Zion, Y. Variations of earthquake properties before, during, and after the 2019 M7.1 Ridgecrest, CA, earthquake. *Geophys. Res. Lett.* **47**, e2020GL089650 (2020).

15. Wang, K., Dreger, D. S., Tinti, E., Bürgmann, R. & Taira, T. Rupture process of the 2019 Ridgecrest, California Mw 6.4 foreshock and Mw 7.1 earthquake constrained by seismic and geodetic data. *Bull. Seismol. Soc. Am.* **110**, 1603–1626 (2020).

16. Lachenbruch, A. H. & Sass, J. Heat flow and energetics of the San Andreas fault zone. *J. Geophys. Res. Solid Earth* **85**, 6185–6222 (1980).

17. Ulrich, T., Gabriel, A.-A., Ampuero, J.-P. & Xu, W. Dynamic viability of the 2016 Mw 7.8 Kaikōura earthquake cascade on weak crustal faults. *Nature Communications* **10**, 1213 (2019).

18. Li, B. & Ghosh, A. Imaging rupture process of the 2015 Mw 8.3 Illapel earthquake using the US seismic array. In *The Chile-2015 (Illapel) Earthquake and Tsunami*, 33–43 (Springer, 2017).

19. Hallo, M. & Gallovič, F. Bayesian self-adapting fault slip inversion with Green's functions uncertainty and application on the 2016 Mw7.1 Kumamoto earthquake. *J. Geophys. Res. Solid Earth* **125**, e2019JB018703 (2020).

20. Carena, S. & Suppe, J. Three-dimensional imaging of active structures using earthquake aftershocks: the Northridge thrust, California. *J. Geol. Soc.* **24**, 887–904 (2002).

21. Liang, C., Ampuero, J.-P. & Pino Muñoz, D. Deep ductile shear zone facilitates near-orthogonal strike-slip faulting in a thin brittle lithosphere. *Geophys. Res. Lett.* **48**, e2020GL090744 (2021).

22. Lee, E.-J. *et al.* Full-3-D tomography for crustal structure in Southern California based on the scattering-integral and the adjoint-wavefield methods. *J. Geophys. Res. Solid Earth* **119**, 6421–6451 (2014).

374 23. Yang, W. & Hauksson, E. The tectonic crustal stress field and style of faulting along the
375 Pacific North America Plate boundary in Southern California. *Geophys. J. Int.* **194**, 100–
376 117 (2013).

377 24. Verdecchia, A. & Carena, S. Coulomb stress evolution in a diffuse plate boundary: 1400
378 years of earthquakes in eastern California and western Nevada, USA. *Tectonics* **35**, 1793–
379 1811 (2016).

380 25. Copley, A. The strength of earthquake-generating faults. *J. Geol. Soc.* **175**, 1–12 (2017).

381 26. Di Toro, G. *et al.* Fault lubrication during earthquakes. *Nature* **471**, 494–498 (2011).

382 27. SCEDC. Southern California Earthquake Data Center (2013). URL `https://scedc.`
383 `caltech.edu`.

384 28. Goldberg, D. E. *et al.* Complex rupture of an immature fault zone: A simultane-
385 ous kinematic model of the 2019 Ridgecrest, CA earthquakes. *Geophys. Res. Lett.* **47**,
386 e2019GL086382 (2020).

387 29. Liu, M., Zhang, M., Zhu, W., Ellsworth, W. L. & Li, H. Rapid characterization of the July
388 2019 Ridgecrest, California, earthquake sequence from raw seismic data using machine-
389 learning phase picker. *Geophys. Res. Lett.* **47**, e2019GL086189 (2020).

390 30. Liu, C., Lay, T., Brodsky, E. E., Dascher-Cousineau, K. & Xiong, X. Coseismic rupture
391 process of the large 2019 Ridgecrest earthquakes from joint inversion of geodetic and seis-
392 mological observations. *Geophys. Res. Lett.* **46**, 11820–11829 (2019).

393 31. Lozos, J. C. & Harris, R. A. Dynamic rupture simulations of the M6.4 and M7.1 July 2019
394 Ridgecrest, California, earthquakes. *Geophys. Res. Lett.* **47**, e2019GL086020 (2020).

32. Cortez, J. T. *et al.* On the rupture propagation of the 2019 M6.4 Searles Valley, California, earthquake, and the lack of immediate triggering of the M7.1 Ridgecrest earthquake. *Geophys. Res. Lett.* **48**, e2020GL090659 (2021).

33. Milliner, C. & Donnellan, A. Using daily observations from Planet Labs satellite imagery to separate the surface deformation between the 4 July Mw 6.4 foreshock and 5 July Mw 7.1 mainshock during the 2019 Ridgecrest earthquake sequence. *Seismol. Res. Lett.* **91**, 1986–1997 (2020).

34. Gabriel, A.-A., Ampuero, J.-P., Dalguer, L. A. & Mai, P. M. The transition of dynamic rupture styles in elastic media under velocity-weakening friction. *J. Geophys. Res.* **117**, B09311 (2012).

35. Melgar, D. *et al.* Real-time high-rate GNSS displacements: performance demonstration during the 2019 Ridgecrest, California, earthquakes. *Seismol. Res. Lett.* **91**, 1943–1951 (2019).

36. Baltzopoulos, G., Luzi, L. & Iervolino, I. Analysis of near-source ground motion from the 2019 Ridgecrest earthquake sequence. *Bull. Seismol. Soc. Am.* **110**, 1495–1505 (2020).

37. Toda, S. & Stein, R. S. Long- and short-term stress interaction of the 2019 Ridgecrest sequence and Coulomb-based earthquake forecasts. *Bull. Seismol. Soc. Am.* **110**, 1765–1780 (2020).

38. Garagash, D. I. Fracture mechanics of rate-and-state faults and fluid injection induced slip. *Phil. Trans. R. Soc. A.* **379**, 20200129 (2021).

39. Yue, H. *et al.* The 2019 Ridgecrest, California earthquake sequence: evolution of seismic and aseismic slip on an orthogonal fault system. *Earth Planet Sci. Lett.* **570**, 117066 (2021).

40. Premus, J., Gallovič, F. & Ampuero, J.-P. Bridging time scales of faulting: from coseismic to postseismic slip of the Mw 6.0 2014 South Napa, California earthquake. *Sci. Adv.* **8**, eabq2536 (2022).

41. Ponti, D. J. *et al.* Documentation of surface fault rupture and ground-deformation features produced by the 4 and 5 July 2019 Mw 6.4 and Mw 7.1 Ridgecrest earthquake sequence. *Seismol. Res. Lett.* **91**, 2942–2959 (2020).

42. Rodriguez Padilla, A. M. *et al.* Near-field high-resolution maps of the Ridgecrest earthquakes from aerial imagery. *Seismol. Res. Lett.* **93**, 494–499 (2021).

43. Taufiqurrahman, T., Gabriel, A.-A., Ulrich, T., Valentova, L. & Gallovič, F. Broadband dynamic rupture modeling with fractal fault roughness, frictional heterogeneity, viscoelasticity and topography: the 2016 Mw 6.2 Amatrice, Italy earthquake. *Geophys. Res. Lett.* 31 (2022).

44. Antoine, S. L. *et al.* Diffuse Deformation and Surface Faulting Distribution from Submetric Image Correlation along the 2019 Ridgecrest, California, Ruptures. *Bull. Seismol. Soc. Am.* **111**, 2275–2302 (2021).

45. Wang, X. & Zhan, Z. Seismotectonics and fault geometries of the 2019 Ridgecrest sequence: Insight from aftershock moment tensor catalog using 3-D Green's functions. *J. Geophys. Res. Solid Earth* **124**, e2020JB019577 (2020).

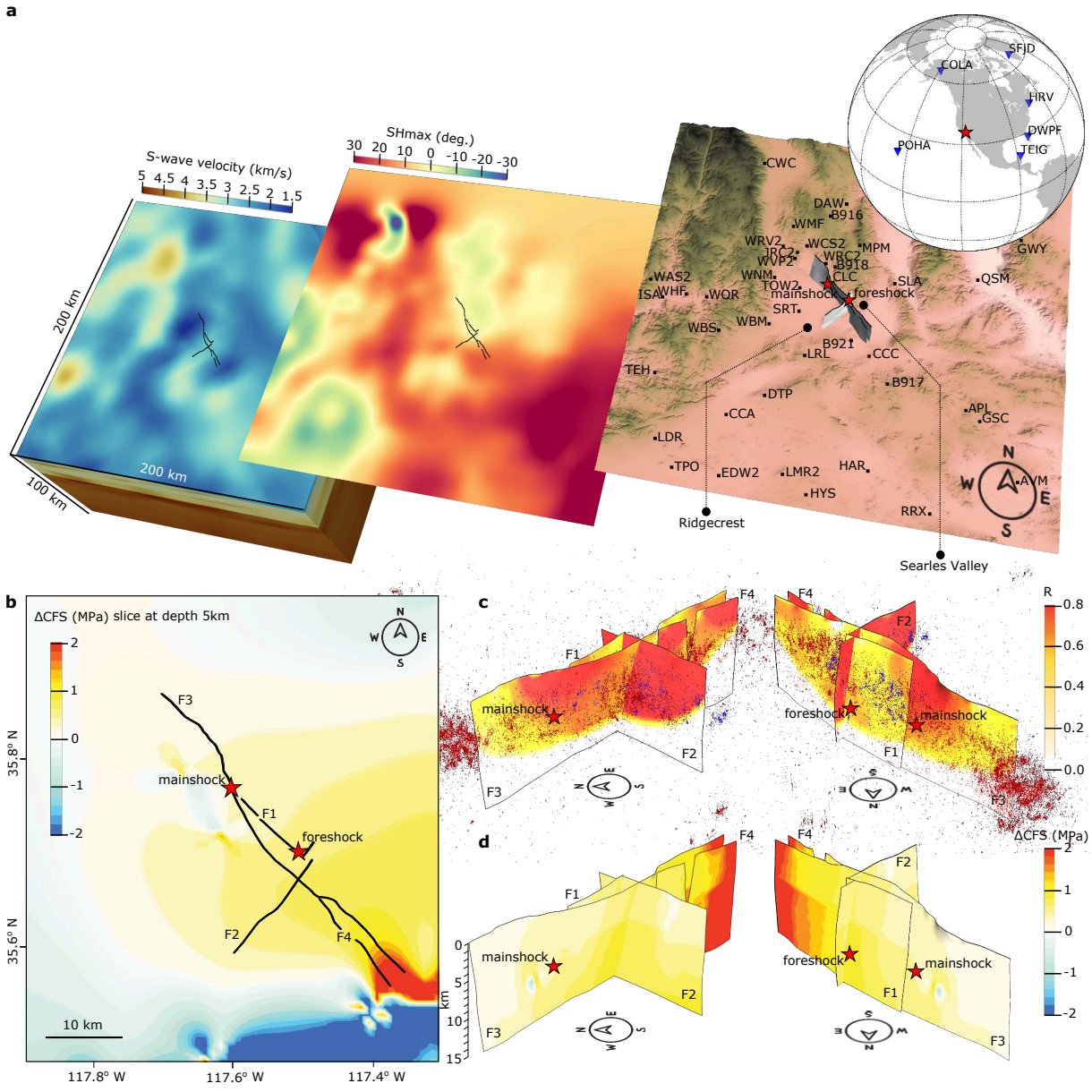

Figure 1: **Observational constraints for 3D dynamic rupture modeling of the Ridgecrest earthquake sequence.** (a) 3D S-wave velocity model (left, CVM-S4.26 (*22*)), 2D model of maximum horizontal stress orientation $SH_{\max}$ (middle, YHSM-2013 (*23*)) and the study region with geometrically-complex fault network (black lines) intersecting topography from SRTM DEM data (right). Chosen strong-motion (black squares) and teleseismic (blue triangles) station locations. (b) 3D cumulative Coulomb failure stress change ΔCFS due to major historical and recent earthquakes (see Table S1, see Methods), sliced at 5 km depth. (c) Two perspectives of the relative prestress ratio R, which is modulated by fault geometry and heterogeneous ambient stress. Blue and red dots are relocated hypocenters of foreshock and mainshock aftershocks (*1*), red stars are foreshock and mainshock hypocenter locations (*27*). (d) ΔCFS resolved on the fault network, assuming a rake of -170° on fault segments F1, F3, and F4; and 0° on F2.

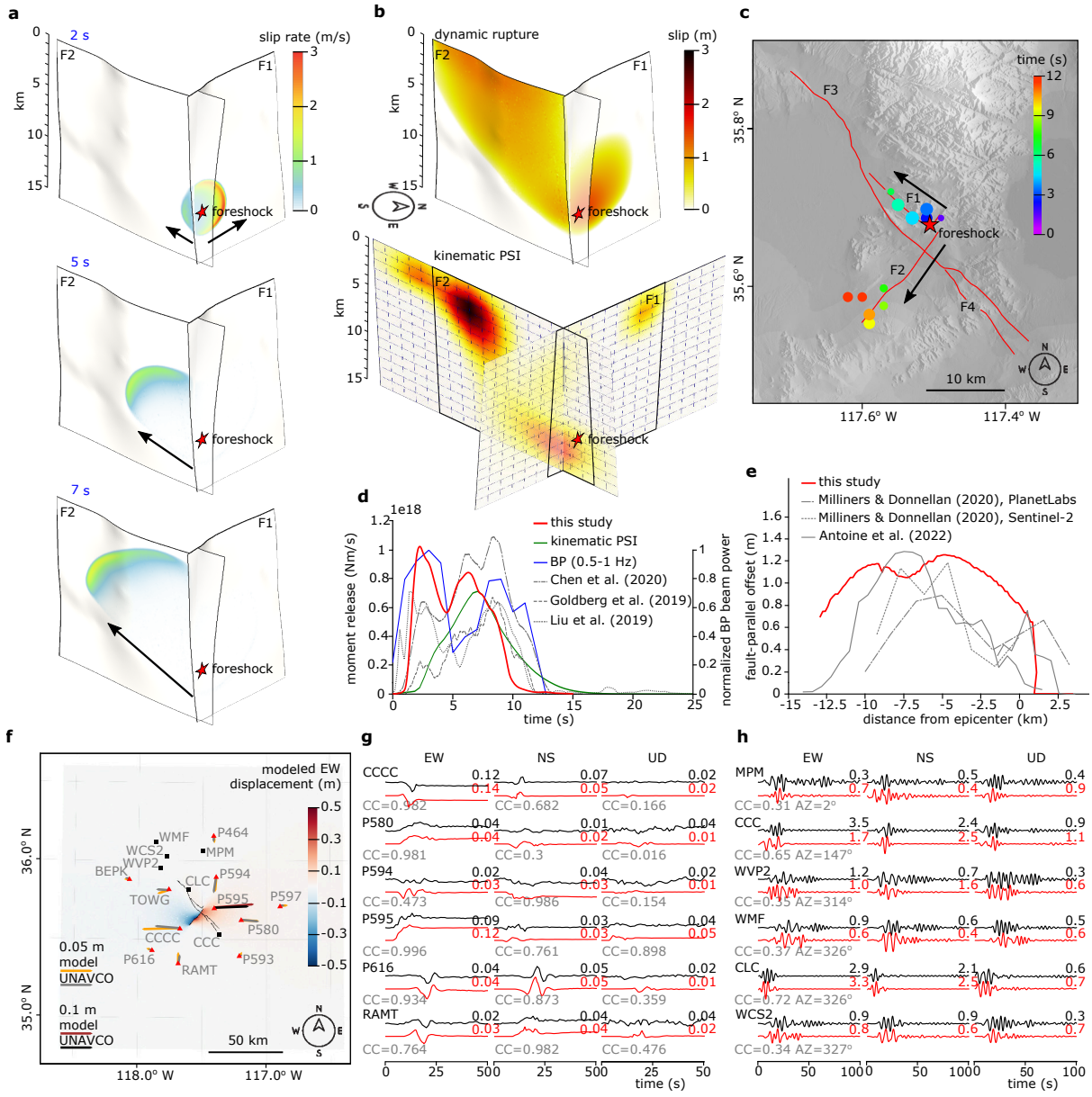

Figure 2: **Dynamic rupture scenario of the Searles Valley foreshock and comparison to observations.** (a) Snapshots of absolute slip rate (see also Video S1). (b) Fault slip of the dynamic rupture model (top) and kinematic parametric source inversion (PSI, bottom). (c) Aftershock-calibrated back-projection (0.5-1 Hz). Black arrows show rupture directions. (d) Dynamic rupture moment release rate and back-projection beam power compared to kinematic models (*8, 28, 29*) including PSI. (e) Fault-parallel surface offsets along F2 (red is dynamic rupture model measured orthogonally across the fault trace 400 m from it, grey is from optical images using orbits of PlanetLabs and Sentinel-2 (*33*)), and on-fault slip estimated from high-resolution optical satellite image correlation (*44*). (f) Horizontal co-seismic surface deformation. Orange and red vectors are the modelled static horizontal displacements scaled by 0.05 m and 0.1 m. Gray and black vectors show UNAVCO processed data. Red triangles and black squares are GPS and strong motion stations shown in (g) and (h). (g) Comparison of 1 Hz continuous GPS observations (*35*) (black) and synthetics (red), component-wise cross-correlation coefficients (CC, gray, see Methods). (h) Comparison between synthetic (red) and recorded regional seismograms (black), band-pass filtered between 0.1-0.3 Hz, sorted by their azimuth relative to the foreshock epicenter. CC (gray) from 300 s three component waveforms. All time series in (g) and (h) are normalized by peak amplitudes (values top right).

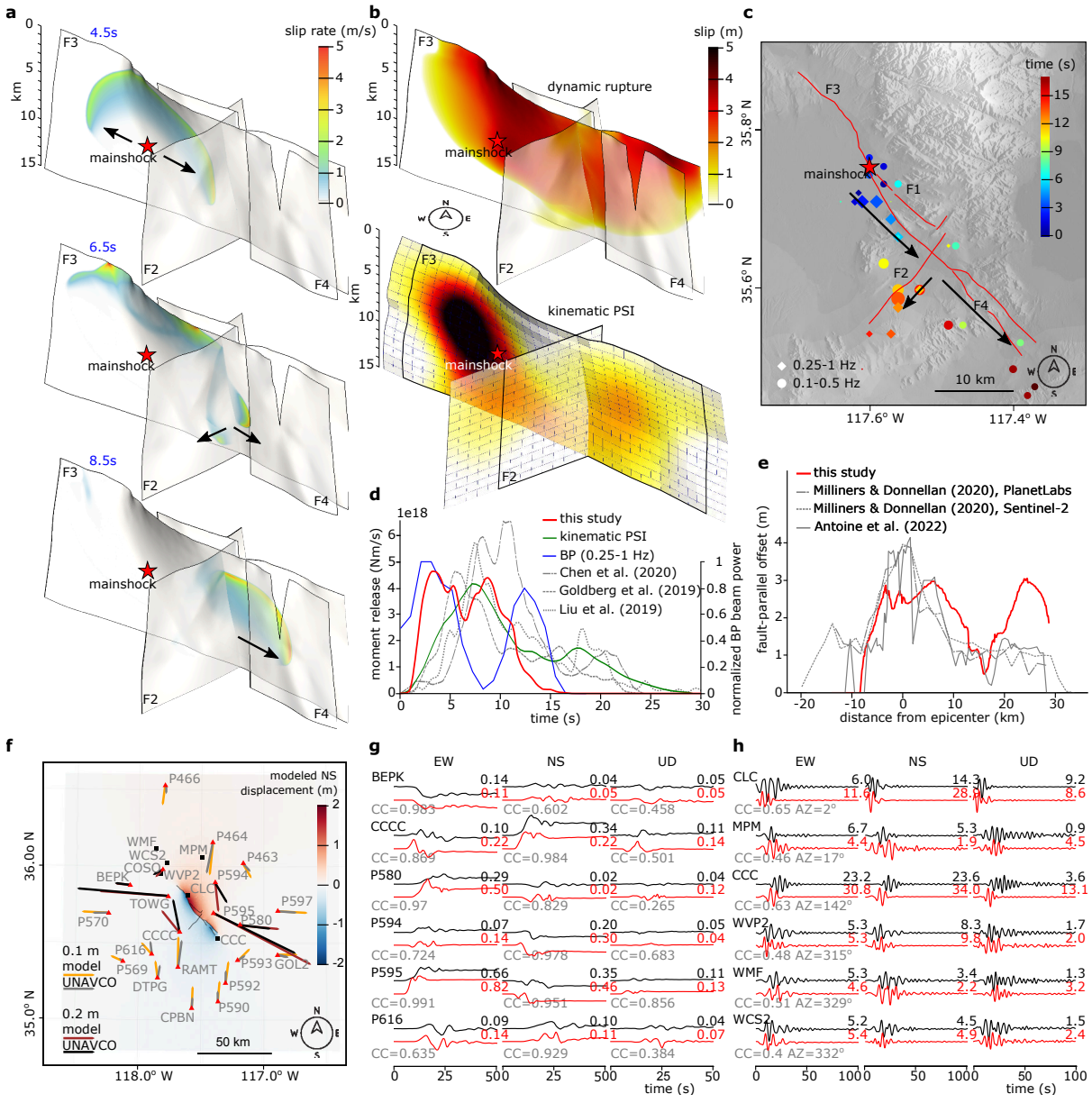

Figure 3: **Dynamic rupture scenario of the Ridgecrest mainshock and comparison to observations.** Details are the same as in Fig. 2. (a) Snapshots of absolute slip rate (see also Video S2). (b) Fault slip of the dynamic rupture model (top) and kinematic PSI (bottom). (c) Aftershock-calibrated back-projection (based on 0.1-0.5 Hz and 0.25-1 Hz frequency bands, respectively). (d) Dynamic rupture moment release rate and back-projection beam power compared to kinematic models. (e) Fault-parallel surface offsets along F3. (f) Horizontal (NS) co-seismic surface deformation. Synthetic horizontal displacement vectors are scaled by 0.1 m and 0.2 m and the underlying map view shows modeled NS displacements. (g) Comparison of synthetic (red) and 1 Hz continuous GPS observations (*35*) (black). (h) Comparison between synthetic (red) and recorded regional seismograms (black).

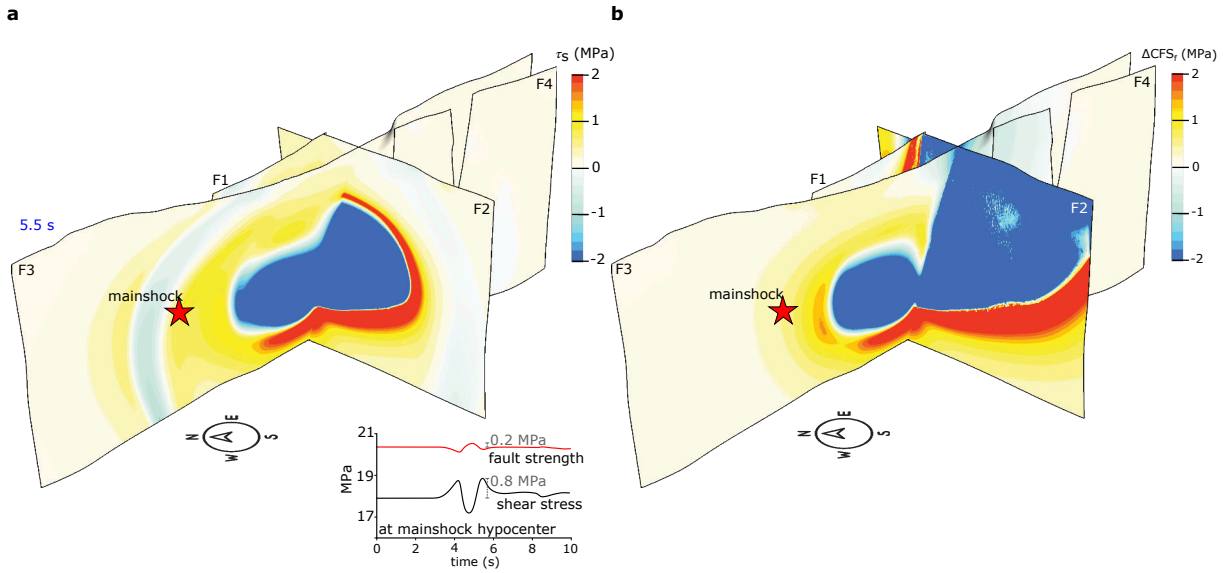

Figure 4: **Co- and postseismic stress changes.** (a) Along-strike dynamic shear stress perturbation after 5.5 s of foreshock dynamic rupture. Inset: Evolution of dynamic shear stress and fault strength during the first 10 s of foreshock dynamic rupture at the mainshock hypocenter (red star). (b) Post-foreshock scalar Coulomb failure stress changes $\Delta\mathrm{CFS}_f$ calculated as: $\Delta\mathrm{CFS}_f = \Delta\tau - f^{'}\Delta\sigma_\mathrm{n}$, $\Delta\tau$ and $\Delta\sigma_\mathrm{n}$ are the total shear and normal fault stress change, $f^{'} = f(1-\gamma) = 0.4$ is the effective friction coefficient. The color bar is saturated at ± 2 MPa.

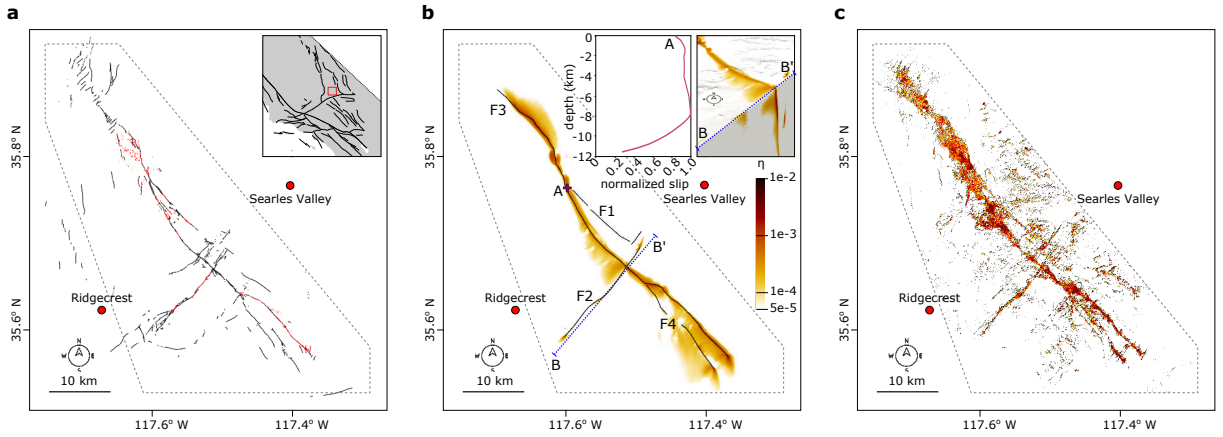

Figure 5: **Off-fault surface deformation and shallow slip deficit (SSD).** (a) Surface rupture mapping from field observations (black, (*41*)) and high-resolution aerial imagery (red, (*42*)). Inset: location within the ECSZ. (b) Modeled off-fault plastic strain, quantified as η (see Methods). Inset: (left) Depth profile of normalized slip at the epicenter (red cross at A). (right) Cut-away view combining a map view and a vertical slice through the flower-like damage zone (accumulated off-fault plastic strain η). (c) Damage Proxy Map (DPM) (*1*) generated from pre- and postseismic InSAR coherence data.

Methods

Numerical method

We solve the non-linearly coupled spontaneous dynamic rupture and seismic wave propagation problem with high-order accuracy in space and time using the open-source software SeisSol (`https://github.com/SeisSol/SeisSol`),. SeisSol uses the Arbitrary high-order accurate DERivative Discontinuous Galerkin method (ADER-DG) (*111*) and end-to-end optimization for high-performance computing (HPC) infrastructure (*112–116*). SeisSol employs fully non-uniform unstructured tetrahedral meshes that statically adapt to geometrically complex 3D geological structures, such as non-planar mutually intersecting faults and topography. SeisSol is verified in a wide range of community benchmarks (*117*) by the SCEC/USGS Dynamic Rupture Code Verification project (*118*), (*46*).

We link the foreshock and mainshock dynamic rupture earthquake models in the same simulation to account for the dynamic and static stress changes of the foreshock rupture in our scenario of the mainshock. Due to the lack of intermediate, spontaneous dynamic triggering of the mainshock in our models, we quantify the required additional prestress to iniate the mainshock at the mainshock hypocenter at 100 s after initiating the foreshock. This time span ensures that all transient seismic waves emitted during the foreshock have left the model domain.

Fault geometry

We use a surface fitting technique (*20*) to generate a 3D geometric model independently of a priori structural interpretation of the conjugate fault network that may have ruptured during the 2019 Ridgecrest sequence (Fig. S1a). Our fault model is based on relocated earthquake hypocenter locations (*1*) combined with earthquake focal mechanisms (*27*) and fault surface traces. We map fault surface traces from a combination of InSAR data (*47*), public satellite imagery (`earth.google.com/web/`) where pre- and post-earthquake images can be com-

pared, private satellite imagery (*48*), and digital elevation models (`apps.nationalmap.gov/viewer/`). To map the foreshock faults, we only use hypocenters and focal mechanisms of those events that occurred in-between the foreshock and mainshock. For the mainshock faults, we only use aftershocks that occurred during the first 48 hr after the mainshock. Surface traces are set as 3D fixed constraints. We use the software SKUA-GOCAD as modeling environment. The model is composed of four geometrically complex fault segments (Figs. 1, S1a): three NW-SE trending faults (F1, F3, and F4) and a conjugate NE-SW trending segment (F2). The largest fault, F3, is $\sim$45 km long (Fig. S1a). Its dip varies from $\sim$80° SW in its northern part to $\sim$70° NE south of the mainshock hypocenter, which results in a helical fault geometry (*21, 45*). F1, a $\sim$15 km long segment parallel to F3, and F2, a $\sim$20 km long conjugate segment, are the main structures dynamically activated during the foreshock. F4 is a $\sim$15 km long branch in the southwest of F3, and F2, F3 and F4 all slip dynamically during the mainshock. Our constructed faults align with the updated Southern California Earthquake Center (SCEC) Community Fault Model (CFM, version 5.3, `https://zenodo.org/record/5899364`, Fig. S1b), including fault representations for the Ridgecrest earthquake sequence (*49*). We omit secondary features, such as smaller orthogonal faults that appear as shallow lineations in seismicity (*1*) and space geodesy (*50*) (Fig. S1). Our modeled distributed off-fault plastic strain, however, aligns with regions of observed off-fault damage (Fig. 5).

Fault friction

We adopt a strong velocity-weakening rate-and-state friction law (*46, 51*) that allows reproducing the severe reduction of co-seismic friction observed in laboratory experiments at high slip rates (*26*). With this friction law, our fault system is operating at low average shear stress (Fig. S5) while dynamically yielding reasonable levels of fault slip and stress drop. This friction law also facilitates rupture cascading across the conjugate fault network and co-seismic com-

plexity such as rupture pulse-to-crack transition and coseismic restrengthening (*52, 53*) (*34*).

In a rate-and-state framework, frictional fault strength depends upon the state of the fault surface as well as the current slip rate (*54, 55*). The strength of each fault is assumed to be proportionate to the magnitude of shear traction τ,

$$\tau = f(V, \Psi)\sigma_{\mathrm{n}}', \tag{1}$$

where f is the effective friction coefficient, V is slip rate, Ψ is the state variable, and σ_{n}' is the effective normal stress. $\boldsymbol{\tau}$ and $\boldsymbol{V}$ are parallel and satisfy $\tau\boldsymbol{V} = V\boldsymbol{\tau}$. The instantaneous friction coefficient f depends on V and Ψ and is computed as

$$f(V, \Psi) = a\ \sinh^{-1}(\frac{V}{2V_0}\exp(\frac{\Psi}{a})), \tag{2}$$

where a is the direct-effect parameter and V_0 is the reference velocity. The evolution of Ψ is governed by

$$\frac{d\Psi}{dt} = -\frac{V}{L}(\Psi - \Psi_{\mathrm{ss}}(V)), \tag{3}$$

where Ψ_{ss} is the steady-state value of the state variable and is given by

$$\Psi_{\mathrm{ss}} = a\ \ln(\frac{2V_0}{V}\sinh(\frac{f_{\mathrm{ss}}(V)}{a})). \tag{4}$$

The steady-state friction coefficient f_{ss} is

$$f_{\mathrm{ss}}(V) = f_{\mathrm{w}} + \frac{f_{\mathrm{LV}}(V) - f_{\mathrm{w}}}{(1 + (V/V_{\mathrm{w}})^8)^{1/8}}, \tag{5}$$

where f_{LV} is the low-velocity friction coefficient which depends on f_0 defined as the steady-state low-velocity friction coefficient at V_0, and is given by

$$f_{\mathrm{LV}}(V) = f_0 - (b - a)\ln\frac{V}{V_0}. \tag{6}$$

All frictional parameters we prescribe are listed in Table S2. We note that we do not directly prescribe the maximum static friction coefficient (μ_{s}), which dynamically varies across the fault system and may exceed f_0.

Fig. S4a shows the depth-dependent direct-effect parameter a and constant evolution-effect parameter b. a linearly increases to 4 km depth, such that the fault frictional behavior transitions from velocity-weakening to velocity-strengthening at 1.8 km depth. The assumed increase of $a - b$ at shallow depth is motivated by (i) direct shear and triaxial experiments (*56*) showing temperature dependence of this parameter, (ii) models reproducing the variability of shallow creep behaviour in both postseismic and interseismic periods (*57*) and (iii) previous dynamic rupture modeling (*58*).

Prestress

We construct an ambient 3D heterogeneous prestress combining observations with simple theoretical analysis and community models.

2D community stress model

We adapt stress as a normalized zero-trace tensor S_{ij} from a 2D community stress model (YHSM-2013 (*23*), provided by the Southern California Earthquake Center, `https://scec.org/research/csm/`). The YHSM-2013 community stress model is based on damped stress inversion from high-quality SCSN earthquake focal mechanisms from 1981-2010 (*23*) and provides the time-averaged regional lateral variation of the maximum horizontal compressional stress $SH_{\max}$ and the stress shape ratio ν in our model domain (Fig. S2). Stress orientations vary on a range of length scales. Similar to other community stress models, YHSM-2013 can resolve the regional larger-scale heterogeneity (5-10 km) of the ambient stress state, but lacks resolution for local stress heterogeneity at smaller scales. We use 0.02° (about 2 km) interpolated YHSM-2013 data. Using inverse multiquadratic radial basis function interpolation and a Gaussian filter with a standard deviation for the Gaussian kernel of σ=2 we smooth any sharp transitions within the stress model.

The stress shape ratio ν describes different faulting mechanisms depending on the eigenvalues (S_1, S_2, and S_3; ordered from most compressional to most tensional) of the ambient stress tensor S_{ij}, with

$$\nu = \frac{S_2 - S_3}{S_1 - S_3}. \tag{7}$$

When S_2 is vertical, as inferred for the Ridgecrest earthquake region (*23*), $\nu < 0.5$ characterizes a transpressional regime, $\nu = 0.5$ characterizes a pure strike-slip regime, and $\nu > 0.5$ characterizes a transtensional regime.

Relative fault strength

We use a systematic approach that allows us to constrain the orientation of all principal stresses, the magnitudes of deviatoric stresses (*17*), and that extends the Mohr-Coulomb theory of frictional failure with dynamic parameters while reducing the large parameter space common in dynamic rupture modeling (*59*). We assume that the ambient prestress is 3D heterogeneous and always Andersonian (*60*), i.e. one principal stress component (S_2) is vertical. We then combine this with the relative fault strength R (*61*), which is the ratio of the potential stress drop to the full breakdown strength drop. R is defined as

$$R = \frac{\tau - \mu_d \sigma_n'}{(\mu_s - \mu_d)\sigma_n'}. \tag{8}$$

$R_0 = 1$ indicates a critical prestress level on all optimally-oriented faults. To compute R we assume $\mu_d \approx f_w$, as we observe that the fully weakened friction is typically reached in our simulations, and $\mu_s \approx f_0$ as a conservative assumption, thus,

$$R \approx \frac{\tau - f_{\mathrm{w}} \sigma_n'}{(f_0 - f_{\mathrm{w}})\sigma_n'}. \tag{9}$$

We note that both approximations may result in locally slightly smaller R than the one we report in Fig. 1c for the preferred rupture models and in Fig. S17 for alternative scenarios not accounting for the long-term ΔCFS.

The absolute magnitude of all principal stresses can then be fully described by (i) the maximum relative fault strength R_0 of virtual fault segments optimally oriented in the stress field, which constrains the smallest and largest principal stress components, (ii) the pore fluid pressure ratio γ, describing overpressurized fault zone fluids (*62*), and modulating effective normal stress σ_n' gradients (*63*), with a hydrostatic state defined as $\gamma = \rho_{\mathrm{water}}/\rho = 0.37$ and higher values of γ corresponding to overpressurized pore fluids and (iii) the stress shape ratio ν.

We compute an ambient depth-dependent prestress tensor, b_{ij}, constrained by $SH_{\max}$, ν, R_0, and γ, by assuming the vertical stress as

$$\sigma_{zz} = \int_0^z \rho(x,y,z')g\,dz' = g\int_0^z \rho(x,y,z')\,dz' = \bar{\rho}(x,y,z)gz, \tag{10}$$

with $\bar{\rho}(x,y,z) = \frac{1}{z}\int_0^z \rho(x,y,z')\,dz'$ being the density of the 3D heterogeneous overburden (based on the here used CVM-S4.26 velocity model (*22*)). Fluid pressure is then assumed to be proportional to vertical stress σ_{zz} as $P_f = \gamma\sigma_{zz}$ and the effective vertical stress is $\sigma_{zz}' = (1-\gamma)\sigma_{zz}$.

Long-term Coulomb failure stress changes (ΔCFS)

We add to the ambient depth-dependent prestress tensor b_{ij}, defined in the previous section, the contribution c_{ij} of coseismic and postseismic Coulomb failure stress changes (ΔCFS) caused by major historical earthquakes ($M_{\mathrm{w}} \geq 7$) that have occurred in the ECSZ during the last $\sim$1400 years (*24*), as well as by recent events of smaller magnitude.This new static stress change model (Fig. S20, Table S1) accounts for 8 additional historical and recent events compared to earlier published versions (*24*).

Figs. 1b and S21a show the associated changes in Coulomb failure stress ΔCFS at 5 km depth, assuming a NW-striking fault plane with strike=318°, dip=88°, and rake=-170°. Prior to the start of the 2019 Ridgecrest sequence, the computed ΔCFS is $\sim$0.8 MPa at the location of the foreshock hypocenter, but only $\sim$0.4 MPa at the mainshock hypocenter. We include the

two largest events (M_{w} 5.8 and M_{w} 4.9) of the 1995 Ridgecrest earthquake sequence, which reduces prestress near the mainshock hypocenter (Fig. 1d). We isolate the contribution of the two 1995 earthquakes by calculating ΔCFS due to only these two events and ΔCFS due to all others (Fig. S21). Both occurred in close proximity to the fault system without causing clear surface rupture (*64*). The effects of the 1995 M_{w} 5.8 and M_{w} 4.9 events are overall local but shadow the hypocentral area of the mainshock, potentially contributing to the delayed triggering. Including previous events in particular on the Garlock fault, leads to positive Coulomb failure stress changes in the foreshock hypocentral area.

We note that we take into account both co- and post-seismic stress changes due to viscoelastic relaxation of the lower crust and upper mantle, which are thought to play an important role at timescales longer than 5 years (*65*). Also, we reiterate that we do not compute ΔCFS on an a priori assumed planar fault geometry, but use a full tensor, which allows us to account for the complexity of the conjugate fault network when resolving on-fault stress changes.

Combined 3D heterogeneous prestress for dynamic rupture modeling

The full prestress tensor s_{ij} used in our dynamic rupture models is obtained by combining the ambient prestress tensor b_{ij} and the pre-Ridgecrest long-term stress change tensor c_{ij}. In addition, we apply a depth-modulation function $\Omega(z)$ (Fig. S4b), which smoothly tapers deviatoric stresses below the spatially-varying seismogenic depth z_{seis} as:

$$s_{ij}(x,y,z) = \Omega(z)(b_{ij}(x,y,z)) + c_{ij}(x,y,z)) + (1-\Omega(z))\sigma'_{\mathrm{zz}}(x,y,z)\delta_{ij}, \qquad (11)$$

with z_{seis} constrained by aftershock locations (Fig. S3). Aditional modulation of the depth-dependence of R_0 would allow to account for potential stress concentrations at the bottom of the seismogenic zone induced by deep creep (*17, 21*). However, the shape and depth of such stress concentration would be difficult to constrain for our complex fault system.

By performing a few dynamic rupture experiments, we find optimal values of γ and R_0, constrained by the mechanic viability of rupture to cascade along the fault network with realistic amounts of fault slip and stress drop. An approximation of the order of magnitude of the expected dynamic stress drop is $R_0(1-\gamma)\sigma_{zz}(f_0 - f_{\mathrm{w}})$, with $f_0 = 0.6 \approx \mu_s$ the static friction coefficient and $f_{\mathrm{w}} = 0.1 \approx \mu_d$ the fully weakened friction, which demonstrates dynamic trade-offs between R_0 and γ (*17*).

We find that a prescribed R_0= 0.8, as the relative strength of an optimal fault in the complex stress field s_{ij}, is a large enough value to allow for sustained foreshock and mainshock rupture along the conjugate fault system, but small enough to reproduce realistic fault slip and stress drop. For the foreshock, we find that a fluid pressure ratio of $\gamma = 0.83$, well below lithostatic but above hydrostatic, produces spontaneous rupture of both F1 and F2 with an amount of fault slip consistent with inversion studies (*8, 28*). In comparison, a mainshock dynamic rupture simulation based on the same γ fails to dynamically rupture the southern parts of F3 and F4. A higher stress drop is needed to sustain rupture beyond the conjugate F2-F3 intersection. We find that reducing fluid pressure by 30% and assuming $\gamma = 0.77$ on F3 and F4, thus allowing for 30% higher potential stress drop than on F1 and F2, allows spontaneous rupture of the southern parts of F3 and F4, well aligned with observations.

Rupture nucleation

In dynamic rupture models, only a small portion, the critical nucleation zone (*66*), of the fault needs to reach failure to nucleate a rupture while faults can be prestressed well below critical (Fig. S5) and yet break spontaneously. Dynamic rupture simulations typically use prescribed nucleation procedures. 3D earthquake cycle simulations that incorporate spontaneous (aseismic) nucleation and dynamic rupture exist (*67–70*) but are methodologically and computationally challenging at the same level of combined geometrical, frictional and structural

complexity (*71, 72*).

Several techniques for nucleating dynamic earthquake ruptures exist, including locally either elevated shear stress, low (effective) static frictional strength or time-weakening forced rupture (*73–76*). We carefully follow established modeling best-practices (*46, 77*), using a nucleation patch smoothly varying in space and time and acting across a minimal-sized perturbation area, avoiding artifacts and initiating self-sustained spontaneous rupture with minimal perturbation determined in several trial dynamic rupture simulations. In both the foreshock and mainshock scenarios spontaneous dynamic rupture is initiated by progressively increasing on-fault shear traction in a spherical volume of radius $r_{\mathrm{nuc}} = 3.5\ \mathrm{km}$ centered at their respective hypocenters (Table S4). The nucleation overstress $\Delta\tau(r,t)$ is given as:

$$\Delta\tau(r,t) = \tau_{\mathrm{nuc}} F(r) G(t), \tag{12}$$

with τ_{nuc} the peak value of the overstress and r the radius from the hypocenter. $F(r)$ defines the shape of the overstress perturbation:

$$F(r) = \begin{cases} \frac{1}{2}\sum_{n=1}^{2} \exp\left[-\frac{1}{2}\left(\frac{r}{r_{\mathrm{crit}}(n)}\right)^2\right] & r < r_{\mathrm{nuc}} \\ 0 & r \geq r_{\mathrm{nuc}} \end{cases} \tag{13}$$

r_{crit}(n=1) and r_{crit}(n=2) are set to 0.4 km, and 1.6 km, respectively. For both events, we use τ_{nuc} = 18 MPa, which results in an average nucleation stress of $\sim$3 MPa over the circular nucleation area (Fig. S13). $G(t)$ is a smoothed step function given as:

$$G(t) = \begin{cases} \exp\left[\frac{(t-T_{\mathrm{nuc}})^2}{t(t-2T_{\mathrm{nuc}})}\right] & 0 < t < T_{\mathrm{nuc}} \\ 1 & t \geq T_{\mathrm{nuc}} \end{cases} \tag{14}$$

with $T_{\mathrm{nuc}} = 1$ s.

Analytical interpretation of the dynamically-required mainshock nucleation stress

We can interpret the additional shear stress required to activate F3 in our dynamic rupture model using an analytical estimate of the shear stress increase carried by afterslip (*38*), implying interaction of coseismic and postseismic slip and their stresses (*12*). We adapt the analytical 1D estimate of the peak shear stress to normal stress ratio f_{p} carried by transient afterslip (Eq. 2.20 of (*38*)) as

$$f_{\mathrm{p}} \approx f_0 + a \ln \frac{v_r/v_0}{\kappa_0 g(v_{\mathrm{r}}/c_{\mathrm{S}})}, \tag{15}$$

where f_0 is the initial fault stress ratio at the ambient fault sliding velocity V_0, the constant near-field prefactor $\kappa_0 \approx 1$, and the universal function (*78*) $g(v_{\mathrm{r}}/c_{\mathrm{S}}) \approx 1$ for aseismic fronts, v_r is the speed of the transient (afterslip) front, $v_0 = \mu V_0/b\sigma_{\mathrm{n}}$ is a characteristic rupture velocity embodying the dependence on the fault ambient conditions. Assuming v_r to correspond to approximately 3 km in 34 hrs (*1*), $a = 0.01$ and $b = 0.014$ yields a peak shear stress perturbation at the transient front of 2.5-4.5 MPa for ambient fault slip rates $V_0 = 10^{-12} \ldots 10^{-16}$ m/s.

Sensitivity of the dynamic rupture models

We analyse the sensitivity of the modeled foreshock and mainshock rupture dynamics to key modeling ingredients including the chosen ambient stress setup and the 3D long-term stress changes. We observe high sensitivity of foreshock rupture dynamics to regional initial conditions, including its simultaneous conjugate rupture, partial surface rupture and lack of coseismic mainshock triggering. We observe high sensitivity of mainshock rupture dynamics to foreshock slip distributions on F1 and F2, for example, with respect to the mainshock's ability to dynamically overcome the geometric and stress barrier posed by the conjugate F2-F3 fault intersection and activate the southern segment of F3.

Our dynamic rupture scenario of the Ridgecrest mainshock fully accounts for the stress

changes due to the Searles Valley foreshock in addition to long-term Coulomb failure stress changes ΔCFS. We here demonstrate the effects of (i) not incorporating the foreshock stress changes in an alternative mainshock rupture dynamics simulation, shown in Fig. S10 and Video S3, and of (ii) omitting both foreshock stresses and ΔCFS in alternative mainshock rupture dynamics simulation (Fig. S11, Video S4). In both cases, mainshock rupture dynamics are less complex than in the preferred model (Fig. S22). In the mainshock model without the foreshock stress changes, spontaneously accumulating fault slip is overall larger than in the preferred mainshock model, especially on F3 near the conjugate F2-F3 intersection (Fig. S19a). Unlike the preferred model, this scenario features no rupture delay at this intersection. We also see more shallow slip on F2 and F4 and more slip at shallow depth after the F2-F3 intersection. In the alternative mainshock simulation omitting additionally long-term ΔCFS, fault slip is overall lower and specifically reduced at shallow depth (Fig. S19b). We observe less slip to the South of F3, no more slip on F4 and reduced slip on F2. Differences in slip to the South are likely linked to the 1453 M_{w}7.7 event on the Garlock fault (*24*). Rupture duration is here about 2 s shorter, due to the lack of dynamic triggering of F4.

In the alternative combined dynamic rupture models (iii) of foreshock and mainshock presented in Figs. S12, S17 and Videos S5, S6, we do not incorporate the pre-Ridgecrest long-term 3D stress changes ΔCFS. In this way, we evidence the non-negligible effects of ΔCFS from previous important earthquakes on foreshock and mainshock rupture dynamics. Fig. S12 shows the foreshock scenario, which lacks pronounced rupture on F2 (Fig. S19c). Differences in the mainshock slip distribution include non-rupture of F4, similar to model (ii). Slip in the southern F3 region is larger than in model (ii) but still reduced with respect to the reference model and not sufficient to dynamically trigger the F4 segment (Fig. S19d). Differences in the relative prestress ratio R on all faults highlight the effect of long-term ΔCFS on the relative strength of F2 and on the mainshock hypocentral region at F3 (Fig. S17).

Lastly, we analyse the sensitivity to the ambient background stress model by implementing the 3D stress inversion model FM3D (*79*) instead of YHSM-2013 (*23*). YHSM-2013 is a 2D model, which has higher lateral resolution in the Ridgecrest region. The alternative combined dynamic rupture models (iv) of foreshock and mainshock with the same long-term ΔCFS are shown in Fig. S18 and Videos S7, S8. In the FM3D foreshock scenario, both F1 and F2 are ruptured with a higher slip magnitude on F2 compared to the reference scenario (Fig. S19e). In the FM3D mainshock scenario, dynamic rupture on F3 terminates at the conjugate intersection with F2, highlighting the sensitivity of a mechanically viable realistic mainshock scenario to the foreshock rupture dynamics and especially to the rupture extent on F2 (Fig. S19f).

Computational mesh and model resolution

The model domain used to jointly simulate both events accounts for high-resolution topography and is spatially discretized in an unstructured tetrahedral mesh of 27,264,253 million tetrahedral elements. We retrieved topography data from the Shuttle Radar Topography Mission (SRTM, (*80*)) using the SRTM.py python package `https://github.com/tkrajina/srtm.py`. The spatially-adaptive mesh resolution is set to an element edge length of h =75 m close to all faults and gradually coarsened away from the fault surfaces. The mesh is also refined near topography, and set to h =500 m element edge lengths at the free surface. We use the WGS84 / UTM Mercator 11S projection.

Simulating 200 seconds physical simulation time on this computational mesh using high-order basis functions of polynomial order p =4, leading to a 5th order space-time accurate numerical scheme for wave propagation, typically requires $\sim$19.5 hours on 250x48 Skylake cores of the SuperMUC-NG supercomputer (Leibniz Supercomputing Center, Germany). Our chosen h, p resolution resolves the seismic wavefield up to at least 2 Hz in the near source region. Each dynamic rupture element face consists of $(p+2)^2$ Gauss integration points, enabling

sub-elemental resolution of rupture dynamics (*81*). The size of the area behind the rupture front in which shear stress decreases from its static to its dynamic value is the process zone width. In the dynamic rupture models presented, we measure the median process zone width as 6.1 km, while for 95% of the ruptured fault elements it is larger than 515 m, which is well resolved by our chosen discretisation.

3D velocity model and viscoelastic attenuation

We embed all faults in the SCEC 3D velocity model CVM-S4.26 (Fig. 1a), which is based on unmodified 3D tomography (*22*). Our simulations use viscoelastic rheologies to model intrinsic attenuation (*82*). The P-wave and S-wave quality factors (Q_P and Q_S) follow established empirical relationships, assuming Q_S = 50 c_S (for c_S in km/s) and Q_P = 2 Q_S (*83, 84*).

Off-fault plasticity

Our model accounts for non-linear off-fault plasticity (Fig. 5b) which, in combination with near-surface velocity-strengthening behavior, permits realistic estimates of the shallow slip deficit (SSD) and near-field ground motion in the presence of complex fault geometries. We assume a non-associated Drucker-Prager elasto-viscoplastic rheology to model off-fault damage (*81*), parameterized by bulk internal friction coefficient and 3D variable plastic cohesion. We use a uniform bulk friction coefficient of 0.7 and define plastic cohesion C_plast as everywhere proportional to the 3D heterogeneous shear modulus (*85*) $\mu(x, y, z)$ (in Pa):

$$C_\mathrm{plast} = 10^{-4}\mu(x, y, z). \tag{16}$$

The onset of plastic yielding is not instantaneous but governed by viscoplastic relaxation with a relaxation time T_v set to 0.05 s, which ensures convergence of simulation results with mesh refinement (*81*).

In our models, the total seismic moment $M_{0,t}$ is the sum of the moment due to slip on the fault, $M_{0,e}$, and $M_{0,p}$, the moment contribution of distributed off-fault plastic strain quantified as

η, a scalar quantity measuring the accumulated off-fault plastic strain at the end of the foreshock or mainshock dynamic rupture simulations. Following previous analysis (*86–89*) we compute the contribution of plastic strain to the total seismic moment as:

$$M_{0,\mathrm{p}} = \sum_{i=1}^{N} \mu V \eta, \tag{17}$$

with μ being the rigidity, V the volume of each tetrahedral element i and

$$\eta(t) = \int_0^t \sqrt{\frac{1}{2}\dot{\epsilon}_{ij}^p \dot{\epsilon}_{ij}^p}\, \mathrm{d}t, \tag{18}$$

and $\dot{\epsilon}_{ij}^p$ being the inelastic strain rate. The contribution of plastic strain to the total moment is small but non-negligible specifically for the mainshock scenario (where $M_{0,\mathrm{p}}/M_{0,\mathrm{t}} \approx 8\%$).

Back-projection

To image the rupture processes of the Searles Valley foreshock and the Ridgecrest mainshock sequence, we assume a grid of possible source locations covering the latitude range 34°N to 37.5°N, and longitude range -120°W to -116°W, with 0.05° grid spacing in both latitude and longitude. We use the relatively dense array data from Alaska. Only stations with relatively high average coherence (>0.6) of the P-wave are selected to avoid interference of low-quality signals and noise. We use the Ridgecrest mainshock as a reference event and apply a cross-correlation method using 20 s of P-wave onset aligned recordings, filtered between 0.1 to 1 Hz to calculate the waveform coherency. Based on this, 268 stations from the Alaska array are selected. Azimuth coverage ranges from 320° to 348°, and epicentral distances range from 30° to 45°, which ensures that P and S phases are well separated. Stations at regional distance have also been used to perform back-projection of both events (*90*), which is overall in agreement with our results. While regional back-projection is feasible with respect to the short duration of both earthquakes, close proximity and rupture complexity of the sequence may challenge regional

BP resolution and stability. We use the 1D velocity model ak135 (*91*) to calculate theoretical travel times from the source grid to each seismic station. We image the rupture process of both events using a sliding time back-projection technique, with 6 s long time windows and 1 s time steps.

We apply a calibration method (*92*) to reduce location uncertainties, which are mainly due to (non-accounted for) non-constant source depths, heterogeneous 3D velocity structures, and anisotropy along the source to station travel paths. For calibrating, we use 14 earthquakes larger than M_{w}4.5 occurring between July 4th and 12th, 2019, including the foreshock and mainshock events (see Table S3).

For the Searles Valley foreshock, we use low frequency (0.5-1 Hz) data to guarantee high coherence of the wave front. Our back-projection images rupture on F1 for 6 s and rupture on F2 within the following 6 s (Fig. 2c). We interpret that F2 rupture is initiated at the hypocenter jointly with F1 rupture, and that F2 breaks in a continuous manner away from the hypocenter. Dynamic triggering from the west side of F2 is unlikely, given the distance from the hypocenter. Rupture directivity effects from F1 towards the array may result in artificially elevated amplitudes in the filtered frequency range (*93*) rendering the first 6 s of rupture on F2 challenging to resolve. Back-projection results, here and in (*94*), suggest that F1 ruptured at about 1 km/s and F2 at about 1.5 km/s. Beam power reaches its first and higher energy peak at about 2-3 s, during F1 rupture. Then energy radiation drops, aligned with F1 rupture terminating in the dynamic rupture scenario. Beam power reaches a second peak at 8-9 s after the estimated rupture onset, which resembles the dynamic rupture model reaching the south-western end of the F2 segment.

For the Ridgecrest mainshock, the higher signal to noise ratio of recorded waveforms guarantees coherent signals up to 2 Hz, and allows to perform multi-frequency back-projection. Higher frequency (1-2 Hz) BP shows continuous rupture from the epicenter to the southern tip of F3, while lower frequency (0.1-0.5 and 0.25-1 Hz) results show also reactivation of F2

(Fig. 3c). BP beam power features two peaks for multiple frequency ranges. The first peak is associated with rupture on F3 to the North of the conjugate F2-F3 intersection and is more sensitive to higher frequencies. We associate the second peak with the reactivation of F2 and the rupture of the SE segment of F3. The frequency-dependence of our back-projection results is likely due to the effect of rupture directivity and rupture speed variation (*93, 95*). The F3 rupture in backwards-array direction towards the SE, results in lower characteristic frequency at the array because of the Doppler effect. On the other hand, a faster rupture speed can increase the characteristic frequency and counteract the Doppler effect. A faster rupture speed in the SE part of F3 (Fig. S14), crossing the conjugate intersection, is also observed from local array-based back-projection (*90*).

Kinematic Parametric Source Inversion (PSI)

We image rupture kinematics of both events from seismic waveforms using the kinematic Parametric Slip Inversion (PSI) method by (*19*). We use all available seismic stations within 130 km distance from the fault. The rupture is assumed to propagate along prescribed fault segments at spatially variable speed. Slip rates are described as Yoffe functions (*96*) with spatially varying rise times. The slip distribution is parameterized using spline interpolation from a variable set of control points. The rake angles are allowed to vary smoothly. Synthetic waveforms are calculated by discretizing the segments into subfaults of 1.5×1 km and convolving their moment-rate functions with the respective Green's functions precalculated in the GIL7 1D velocity model (*97*) using Axitra (*98*). We band-pass filter both data and synthetics between 0.05 and 0.5 Hz.

The inverse problem is formulated in a Bayesian framework (*19*). The prior probability density function (PDF) on the number of slip control points k follows a reciprocal distribution, $p(k) \propto k^{-1}$. By this means, it serves as "Occam's razor", preferring implicitly simple, localized

slip distributions. Other priors are generally uniform (PDF) in relatively wide ranges (e.g., $\pm$45 degrees for the rake angle). The data uncertainty is described by a multivariate Gaussian function with a full covariance matrix. It includes a component accounting for the uncertainty of Green's functions due to imperfect description of the velocity model (*99*). The posterior samples are obtained by a Markov Chain Monte Carlo (MCMC) method, namely the parallel tempering technique (*100*).

We assume two planar faults for the foreshock, approximating the fault geometries of F1 and F2 for simplicity. The mainshock model includes the two fault segments F2 and F3, and honors the deflected F2 geometry. The results shown in the main text in Figs. 2b and 3b correspond to the best-fitting model and serve as an example from the ensemble of solutions obtained by the MCMC sampling.

While smooth initial conditions lead to relatively smooth slip distribution in the dynamic models, the self-adapting spatial parameterization in the kinematic models tends to localize the slip due to the Occam's razor constraint (as the data does not require otherwise). It is challenging to disentangle fault slip across conjugate fault intersections in kinematic methods due to the proximity of faults and the similar radiation pattern of, e.g., right-lateral F1 and left-lateral F2 segments in the foreshock. Therefore, the uncertainty is more significant for both models in the vicinity of the conjugate fault segment intersection. For example, PSI shows a smaller fault slip on F1 around the hypocenter but a bit larger slip on F2 closer to the surface for the foreshock. Similarly, minor slip patches are rather uncertain due to their little contribution to the waveforms. In some cases, such as the one at the NW end of the foreshock's F1, the inferred slip might be "projected" from coinciding secondary, unaccounted faults.

Geodetic data analysis

We obtained the processed static GPS vector data from UNAVCO (`https://www.unavco.org/highlights/2019/ridgecrest.html`). We compare our modeled surface displacements at selected stations with observational data as shown in Fig. 2f and 3f. To avoid contamination by remnant seismic waves propagating throughout the model domain, we extract the synthetic surface displacements at 100 s after dynamic rupture nucleation in both foreshock and mainshock models. We calculate the maximal possible value of cross-correlation (CC) between the observed and synthetic time series component-wise to account for the different signal-to-noise ratios in the horizontal and vertical components.

Our modeled co-seismic GPS displacements of the Searles Valley foreshock match observational recordings well at most stations, with notable overshooting amplitudes at near-fault stations CCCC and P595 (Fig. 2f). For the mainshock, we also observe overall good agreement except for small overshooting displacements at station P595, P580 and P594 (Fig. 3f). Stations CCCC and P595 are close to the terminations of faults in our prescribed fault geometry, and the observed discrepancies may reflect a more gradual rupture arrest along F2 than captured in our model. Additional discrepancies may by associated with secondary faults off the main fault identified with optical imaging (*50*), (*33*) but not explicitly incorporated in our model.

Teleseismic waveforms

We generate synthetic broadband seismograms at 6 teleseismic stations (of the IU network) around the events (Fig.1a and S9) using the Instaseis (*101*) Green's function database and the PREM model incorporating anisotropic effects and accurate to a shortest period of 2 s. The sources for the synthetic teleseismic waveforms are calculated by translating the fault slip time histories of the foreshock and mainshock dynamic rupture models into a respective double-couple point source, that we then use in Instaseis. The observed teleseismic data were down-

loaded from IRIS using Obspy (*102*).

The teleseismic synthetics fit the foreshock (Fig. S9a, average cross-correlation coefficient of ∼0.73) and mainshock (Fig. S9b, average cross-correlation coefficients ∼0.75) observations well in the long period range considered (50–500 s). The simplifying choice of a 1D PREM-based teleseismic Green's function database may explain some of the remaining differences.

Data availability

All data required to reproduce the earthquake sequence scenarios can be downloaded from `https://zenodo.org/record/6842773`. We provide a detailed README file summarizing the data and data formats provided. Our 3D fault model is available at `https://skfb.ly/oDVGw`. The static GPS data related to the co-seismic rupture of both the foreshock and mainshock are available from UNAVCO (`https://www.unavco.org/highlights/2019/ridgecrest.html`). The continuous GPS dataset (*35*) is available at `https://zenodo.org/record/3366342`. The Instaseis Green's function database that we use to compute teleseismic synthetics is hosted by IRIS at `https://ds.iris.edu/ds/products/syngine/`.

Code availability

All dynamic rupture simulations were performed using SeisSol (`www.seissol.org`), an open-source software freely available to download from `https://github.com/SeisSol/SeisSol/`. The used SeisSol code branch and commit are archived at `https://zenodo.org/record/7642533`, doi:10.5281/zenodo.7642533. The SeisSol Ridgecrest sequence branch is also available on Github (`https://github.com/SeisSol/SeisSol/tree/2019_Ridgecrest_sequence`). Instructions for downloading, installing, and running the code are available in the SeisSol documentation at `https://seissol.readthedocs.`

io/. Downloading and compiling instructions are at https://seissol.readthedocs.io/en/latest/compiling-seissol.html. Instructions for setting up and running simulations are at https://seissol.readthedocs.io/en/latest/configuration.html. Quickstart containerized installations and introductory materials are provided in the docker container and jupyter notebooks at https://github.com/SeisSol/Training. Example problems and model configuration files are provided at https://github.com/SeisSol/Examples, many of which reproduce the SCEC 3D Dynamic Rupture benchmark problems described at https://strike.scec.org/cvws/benchmark_descriptions.html. We use the softwares SKUA-GOCAD (https://pdgm.com/products/skua-gocad/) as modeling environment to produce all 3D fault models and the open-source software ParaView (https://www.paraview.org/) for visualisation.

Methods References

46. Harris, R. A. *et al.* A suite of exercises for verifying dynamic earthquake rupture codes. *Seismol. Res. Lett.* **89**, 1146–1162 (2018).

47. Valkaniotis, S. Subpixel optical correlation co-seismic offsets for the Mw 6.4 and Mw7.1 Ridgecrest, California earthquakes, from Copernicus Sentinel 2 data (2019). URL https://doi.org/10.5281/zenodo.3275073.

48. Planet. Planet data application program interface: in space for life on Earth (2019). URL https://www.planet.com/markets/education-and-research/.

49. Plesch, A., Shaw, J. H., Ross, Z. E. & Hauksson, E. Detailed 3D fault representations for the 2019 Ridgecrest, California, earthquake sequence. *Bull. Seismol. Soc. Am.* **110**, 1818–1831 (2020).

50. Xu, X., Sandwell, D. T. & Smith-Konter, B. Coseismic displacements and surface fractures from Sentinel-1 InSAR: 2019 Ridgecrest earthquakes. *Seismol. Res. Lett.* **91**, 1979–1985 (2020).

51. Dunham, E. M., Belanger, D., Cong, L. & Kozdon, J. E. Earthquake ruptures with strongly rate-weakening friction and off-fault plasticity, part 1: planar faults. *Bull. Seismol. Soc. Am.* **101**, 2296–2307 (2011).

52. Heaton, T. H. Evidence for and implications of self-healing pulses of slip in earthquake rupture. *Phys. Earth Planet. Inter.* **64**, 1–20 (1990).

53. Nielsen, S. & Madariaga, R. On the self-healing fracture mode. *Bull. Seismol. Soc. Am.* **93**, 2375–2388 (2003).

54. Dieterich, J. H. Modeling of rock friction: 1. Experimental results and constitutive equations. *J. Geophys. Res. Solid Earth* **84**, 2161–2168 (1979).

55. Ruina, A. Slip instability and state variable friction laws. *J. Geophys. Res. Solid Earth* **88**, 10359–10370 (1983).

56. Blanpied, M. L., Lockner, D. A. & Byerlee, J. D. Fault stability inferred from granite sliding experiments at hydrothermal conditions. *Geophys. Res. Lett.* **18**, 609–612 (1991).

57. Wei, M., Kaneko, Y., Liu, Y. & McGuire, J. J. Episodic fault creep events in California controlled by shallow frictional heterogeneity. *Nature Geosci.* **6**, 566–570 (2013).

58. Kaneko, Y., Lapusta, N. & Ampuero, J.-P. Spectral element modeling of spontaneous earthquake rupture on rate and state faults: Effect of velocity-strengthening friction at shallow depths. *J. Geophys. Res. Solid Earth* **113**, B09317 (2008).

59. Tinti, E. *et al.* Constraining families of dynamic models using geological, geodetic and strong ground motion data: the Mw 6.5, October 30th, 2016, Norcia earthquake, Italy. *Earth Planet Sci. Lett.* **576**, 117237 (2021).

60. Anderson, E. M. The dynamics of faulting. *Trans. Edinburgh Geol. Soc* **8**, 387–402 (1905).

61. Aochi, H. & Madariaga, R. The 1999 Izmit, Turkey, earthquake: nonplanar fault structure, dynamic rupture process, and strong ground motion. *Bull. Seismol. Soc. Am.* **93**, 1249–1266 (2003).

62. Suppe, J. Fluid overpressures and strength of the sedimentary upper crust. *J. Struct. Geol.* **69**, 481–492 (2014).

63. Madden, E. H., Ulrich, T. & Gabriel, A.-A. The state of pore fluid pressure and 3-D megathrust earthquake dynamics. *J. Geophys. Res. Solid Earth* **127**, e2021JB023382 (2022).

64. Hauksson, E. *et al.* Preliminary report on the 1995 Ridgecrest earthquake sequence in Eastern California. *Seismol. Res. Lett.* **66**, 54–60 (1995).

65. Verdecchia, A. & Carena, S. One hundred and fifty years of Coulomb stress history along the California-Nevada border, USA: Coulomb stress history CA-NV border. *Tectonics* **34**, 213–231 (2015).

66. Rubin, A. M. & Ampuero, J.-P. Earthquake nucleation on (aging) rate and state faults. *J. Geophys. Res. Solid Earth* **110**, B11312 (2005).

67. Lapusta, N. & Liu, Y. Three-dimensional boundary integral modeling of spontaneous earthquake sequences and aseismic slip. *Journal of Geophysical Research: Solid Earth* **114** (2009).

68. Jiang, J. & Lapusta, N. Deeper penetration of large earthquakes on seismically quiescent faults. *Science* **352**, 1293–1297 (2016).

69. Luo, B., Duan, B. & Liu, D. 3d finite-element modeling of dynamic rupture and aseismic slip over earthquake cycles on geometrically complex faults. *Bulletin of the Seismological Society of America* **110**, 2619–2637 (2020).

70. Meng, Q. & Duan, B. Dynamic modeling of interactions between shallow slow-slip events and subduction earthquakes. *Seismological Society of America* **94**, 206–216 (2023).

71. Jiang, J. *et al.* Community-driven code comparisons for three-dimensional dynamic modeling of sequences of earthquakes and aseismic slip. *J. Geophys. Res. Solid Earth* **127**, e2021JB023519 (2022).

72. Uphoff, C., May, D. A. & Gabriel, A.-A. A discontinuous Galerkin method for sequences of earthquakes and aseismic slip on multiple faults using unstructured curvilinear grids. *Geophys. J. Int.* (2022).

73. Andrews, D. Rupture models with dynamically determined breakdown displacement. *Bull. Seismol. Soc. Am.* **94**, 769–775 (2004).

74. Bizzarri, A. How to promote earthquake ruptures: Different nucleation strategies in a dynamic model with slip-weakening friction. *Bull. Seismol. Soc. Am.* **100**, 923–940 (2010).

75. Hu, F., Huang, H. & Chen, X. Effect of the time-weakening friction law during the nucleation process. *Earthq. Sci.* **30**, 91–96 (2017).

76. Harris, R. A. *et al.* A geology and geodesy based model of dynamic earthquake rupture on the Rodgers Creek-Hayward-Calaveras fault system, California. *J. Geophys. Res. Solid Earth* **126**, e2020JB020577 (2021).

946 77. Galis, M. *et al.* On the initiation of sustained slip-weakening ruptures by localized stresses.
947 *Geophys. J. Int.* **200**, 890–909 (2015).

948 78. Freund, L. B. *Dynamic fracture mechanics* (Cambridge University Press, 1998).

949 79. Hardebeck, J. L. & Michael, A. J. Damped regional-scale stress inversions: Methodology
950 and examples for southern California and the Coalinga aftershock sequence. *J. Geophys.*
951 *Res. Solid Earth* **111**, B11310 (2006).

952 80. Farr, T. G. *et al.* The shuttle radar topography mission. *Rev. Geophys.* **45**, RG2004 (2007).

953 81. Wollherr, S., Gabriel, A.-A. & Uphoff, C. Off-fault plasticity in three-dimensional dynamic
954 rupture simulations using a modal Discontinuous Galerkin method on unstructured meshes:
955 implementation, verification and application. *Geophys. J. Int.* **214**, 1556–1584 (2018).

956 82. Uphoff, C. & Bader, M. Generating high performance matrix kernels for earthquake simula-
957 tions with viscoelastic attenuation. In *2016 International Conference on High Performance*
958 *Computing & Simulation (HPCS)*, 908–916 (IEEE, 2016).

959 83. Day, S. M. & Bradley, C. R. Memory-efficient simulation of anelastic wave propagation.
960 *Bull. Seismol. Soc. Am.* **91**, 520–531 (2001).

961 84. Graves, R. W. *et al.* Broadband simulations for Mw 7.8 southern San Andreas earthquakes:
962 ground motion sensitivity to rupture speed. *Geophys. Res. Lett.* **35**, L22302 (2008).

963 85. Roten, D., Olsen, K. B., Day, S. M., Cui, Y. & Fäh, D. Expected seismic shaking in los
964 angeles reduced by san andreas fault zone plasticity. *Geophys. Res. Lett.* **41**, 2769–2777
965 (2014).

966 86. Andrews, D. J. Rupture dynamics with energy loss outside the slip zone. *J. Geophys. Res.*
967 *Solid Earth* **110**, B01307 (2005).

968 87. Ma, S. A physical model for widespread near-surface and fault zone damage induced by
969 earthquakes. *Geochem. Geophys. Geosyst.* **9**, Q11009 (2008).

970 88. Gabriel, A.-A., Ampuero, J.-P., Dalguer, L. A. & Mai, P. M. Source properties of dy-
971 namic rupture pulses with off-fault plasticity. *J. Geophys. Res. Solid Earth* **118**, 4117–4126
972 (2013).

973 89. Ulrich, T., Gabriel, A.-A. & Madden, E. H. Stress, rigidity and sediment strength control
974 megathrust earthquake and tsunami dynamics. *Nature Geosci.* **15**, 67–73 (2022).

975 90. Xie, Y., Bao, H. & Meng, L. Source imaging with a multi-array Local back-projection and
976 its application to the 2019 Mw 6.4 and Mw 7.1 Ridgecrest earthquakes. *J. Geophys. Res.*
977 *Solid Earth* **126**, e2020JB021396 (2021).

978 91. Kennett, B. L. N. & Engdahl, E. R. Traveltimes for global earthquake location and phase
979 identification. *Geophys. J. Int.* **105**, 429–465 (1991).

980 92. Ghosh, A., Vidale, J. E. & Creager, K. C. Tremor asperities in the transition zone control
981 evolution of slow earthquakes. *J. Geophys. Res. Solid Earth* **117**, B10301 (2012).

982 93. Li, B. *et al.* Rupture heterogeneity and directivity effects in back-projection analysis. *J.*
983 *Geophys. Res. Solid Earth* **127**, e2021JB022663 (2022).

984 94. Yang, J., Zhu, H. & Lumley, D. Time-lapse imaging of coseismic ruptures for the 2019
985 Ridgecrest earthquakes using multiazimuth backprojection with regional seismic data and
986 a 3-D crustal velocity model. *Geophys. Res. Lett.* **47**, e2020GL087181 (2020).

987 95. Yin, J. & Denolle, M. A. Relating teleseismic backprojection images to earthquake kine-
988 matics. *Geophys. J. Int.* **217**, 729–747 (2019).

96. Tinti, E., Fukuyama, E., Piatanesi, A. & Cocco, M. A kinematic source-time function compatible with earthquake dynamics. *Bull. Seismol. Soc. Am.* **95**, 1211–1223 (2005).

97. Pasyanos, M. E., Dreger, D. S. & Romanowicz, B. Toward real-time estimation of regional moment tensors. *Bull. Seismol. Soc. Am.* **86**, 1255–1269 (1996).

98. Cotton, F. & Coutant, O. Dynamic stress variations due to shear faults in a plane-layered medium. *Geophys. J. Int.* **128**, 676–688 (1997).

99. Hallo, M. & Gallovič, F. Fast and cheap approximation of Green function uncertainty for waveform-based earthquake source inversions. *Geophys. J. Int.* **207**, 1012–1029 (2016).

100. Sambridge, M. A Parallel Tempering algorithm for probabilistic sampling and multimodal optimization. *Geophys. J. Int.* **196**, 357–374 (2013).

101. van Driel, M., Krischer, L., Stähler, S., Hosseini, K. & Nissen-Meyer, T. Instaseis: instant global seismograms based on a broadband waveform database. *Solid Earth* **6**, 701–717 (2015).

102. Krischer, L. *et al.* ObsPy: a bridge for seismology into the scientific Python ecosystem. *Comput. Sci. Discov.* **8**, 014003 (2015).

103. Scharer, K. M., Biasi, G. P. & Weldon II, R. J. A reevaluation of the Pallett Creek earthquake chronology based on new AMS radiocarbon dates, San Andreas fault, California. *J. Geophys. Res. Solid Earth* **116**, B12111 (2011).

104. McAuliffe, L. J. *et al.* Paleoseismology of the southern Panamint Valley fault: Implications for regional earthquake occurrence and seismic hazard in southern California. *J. Geophys. Res. Solid Earth* **118**, 5126–5146 (2013).

105. Lozos, J. C. A case for historic joint rupture of the San Andreas and San Jacinto faults. *Sci. Adv.* **2**, e1500621 (2016).

106. Lin, J. & Stein, R. S. Stress triggering in thrust and subduction earthquakes and stress interaction between the southern San Andreas and nearby thrust and strike-slip faults. *J. Geophys. Res. Solid Earth* **109**, B02303 (2004).

107. Bawden, G. W. Source parameters for the 1952 Kern County earthquake, California: A joint inversion of leveling and triangulation observations. *J. Geophys. Res. Solid Earth* **106**, 771–785 (2001).

108. Wald, D. J. & Heaton, T. H. Spatial and temporal distribution of slip for the 1992 Landers, California, earthquake. *Bull. Seismol. Soc. Am.* **84**, 668–691 (1994).

109. Ji, C., Wald, D. J. & Helmberger, D. V. Source description of the 1999 Hector Mine, California, earthquake, part II: complexity of slip history. *Bull. Seismol. Soc. Am.* **92**, 1208–1226 (2002).

110. Plesch, A. SKUA macro for focal mechanisms. *Harvard University* (2021). URL `https://scholar.harvard.edu/files/plesch/files/skua_macro_for_focal_mechanisms.pdf`.

111. Dumbser, M. & Käser, M. An arbitrary high-order discontinuous Galerkin method for elastic waves on unstructured meshes — II. The three-dimensional isotropic case. *Geophys. J. Int.* **167**, 319–336 (2006).

112. Breuer, A. *et al.* Sustained Petascale Performance of Seismic Simulations with SeisSol on SuperMUC. In *Supercomputing. ISC 2014. Lecture Notes in Computer Science, vol 8488*, 1–18 (Springer, Cham, 2014).

113. Heinecke, A. *et al.* Petascale high order dynamic rupture earthquake simulations on heterogeneous supercomputers. In *International Conference for High Performance Computing, Networking, Storage and Analysis, SC* (2014).

114. Rettenberger, S., Meister, O., Bader, M. & Gabriel, A.-A. Asagi: A parallel server for adaptive geoinformation. In *Proceedings of the Exascale applications and Software Conference 2016*, EASC '16, 2:1–2:9 (ACM, New York, NY, USA, 2016).

115. Uphoff, C. *et al.* Extreme scale multi-physics simulations of the tsunamigenic 2004 Sumatra megathrust earthquake. In *Proceedings of the International Conference for High Performance Computing, networking, Storage and Analysis, SC 2017* (2017).

116. Krenz, L. *et al.* 3D acoustic-elastic coupling with gravity: the dynamics of the 2018 Palu, Sulawesi earthquake and tsunami. In *Proceedings of the International Conference for High Performance Computing, Networking, Storage and Analysis*, SC '21 (ACM, New York, NY, USA, 2021).

117. Pelties, C., Gabriel, A.-A. & Ampuero, J.-P. Verification of an ADER-DG method for complex dynamic rupture problems. *Geoscientific Model Development* **7**, 847–866 (2014).

118. Harris, R. A. *et al.* Verifying a computational method for predicting extreme ground motion. *Seismol. Res. Lett.* **82**, 638–644 (2011).

Acknowledgements:

We thank two referees and Editor J. VanDecar for their constructive reviews. We thank M. Bader, L. Krenz, S. Wolf, R. Dorozhinskii and the group of hardware-aware algorithms and software for high performance computing at TUM for decade-long collaboration. We thank N. Schliwa, J. Biemiller, C. Nicholson and S. A. Wirp for helpful discussions. We are grateful to S. Antoine for sharing surface offset data. This work was supported by the European Union's Horizon 2020 Research and Innovation Programme (TEAR grant No. 852992) and Horizon Europe (ChEESE-2P grant No. 101093038, DT-GEO grant No. 101058129 and Geo-INQUIRE grant No.101058518), the National Science Foundation (grant No. EAR-2121666), the German Research Foundation (DFG projects GA 2465/2-1, GA 2465/3-1) and the Southern California Earthquake Center (SCEC award 21112). We gratefully acknowledge the Gauss Centre for Supercomputing e.V. (`www.gauss-centre.eu`) for providing computing time on the GCS Supercomputer SuperMUC-NG at Leibniz Supercomputing Centre (`www.lrz.de`), in project pr63qo.

Author Information

Department of Earth and Environmental Sciences, Ludwig-Maximilians-Universität München, Munich, Germany

Taufiq Taufiqurrahman, Alice-Agnes Gabriel, Duo Li, Thomas Ulrich, Bo Li, Sara Carena

Institute of Geophysics and Planetary Physics, Scripps Institution of Oceanography, University of California San Diego, La Jolla, USA

Alice-Agnes Gabriel

Department of Earth and Planetary Sciences, McGill University, Montreal, Quebec, Canada

Alessandro Verdecchia

Institute of Geology, Mineralogy and Geophysics, Ruhr-University Bochum, Bochum, Germany

Alessandro Verdecchia

Department of Geophysics, Faculty of Mathematics and Physics, Charles University, Prague, Czech Republic

Frantisek Gallovic

Author Contributions

Conceptualization, Formal Analysis, Software, Visualization and Writing: Taufiq Taufiqurrahman, Alice-Agnes Gabriel, Duo Li, Thomas Ulrich, Bo Li, Sara Carena, Alessandro Verdecchia and Frantisek Gallovic. Funding Acquisition and Resources: Alice-Agnes Gabriel.

Corresponding author

Correspondence to Alice-Agnes Gabriel, algabriel@ucsd.edu.

Competing interests

The authors declare no competing interests.

Supplementary Information

This file contains Supplementary Tables 1–4, Supplementary Figures 1–22 and legends for Supplementary Videos 1–8.

Video S1: Evolution of absolute slip rate (m/s) across the fault network from 4 perspectives. Preferred foreshock dynamic rupture scenario.

Video S2: Evolution of absolute slip rate (m/s) across the fault network from 4 perspectives. Preferred mainshock dynamic rupture scenario.

Video S3: Evolution of absolute slip rate (m/s) across the fault network from 4 perspectives. Alternative mainshock dynamic rupture scenario not accounting for the dynamic and static foreshock stress changes.

Video S4: Evolution of absolute slip rate (m/s) across the fault network from 4 perspectives. Alternative mainshock dynamic rupture scenario not accounting for the dynamic and static foreshock stress changes and in addition omitting the effects of the long-term ΔCFS.

Video S5: Evolution of absolute slip rate (m/s) across the fault network from 4 perspectives. Alternative foreshock dynamic rupture scenario omitting the long-term ΔCFS.

Video S6: Evolution of absolute slip rate (m/s) across the fault network from 4 perspectives. Alternative mainshock dynamic rupture scenario omitting the long-term ΔCFS.

Video S7: Evolution of absolute slip rate (m/s) across the fault network from 4 perspectives. Alternative foreshock dynamic rupture scenario loaded with an alternative community ambient stress model.

Video S8: Evolution of absolute slip rate (m/s) across the fault network from 4 perspectives. Alternative mainshock dynamic rupture scenario loaded with an alternative community ambient stress model.

Table S1: Past earthquakes incorporated in the pre-Ridgcerest co- and post-seismic cumulative Coulomb failure stress change model ΔCFS. The model of (*24*) has here been updated by incorporating the contribution of 8 additional events, highlighted in blue.

Year	Earthquake	Magnitude
587	Antelope Valley	7.2
700	Pyramid Lake	7.0
913	Fish Lake (Leidy Creek)	6.8
950	Fish Lake (Oasis)	6.7
1170	Benton Springs	7.2
1375	Incline Village	7.1
1508	Mojave (San Andreas)	7.5 (*103, 104*)
1540	Garlock	7.7
1557	Panamint Valley	7.1
1600	Mount Rose	7.0
1605	Genoa	7.2
1715	Furnace Creek	7.2
1812	Wrightwood	7.5 (*105*)
1857	Fort Tejon	7.9 (*106*)
1872	Owens Valley	7.5
1915	Pleasant Valley	7.5
1932	Cedar Mountain	7.2
1952	Kern County	7.3 (*107*)
1954	Rainbow Mountain	7.0
1954	Fairview Peak	7.1
1954	Dixie Valley	7.2
1992	Landers	7.2 (*108*)
1995	Ridgecrest	5.8 & 4.9 (*64*)
1999	Hector Mine	7.1 (*109*)

Table S2: Rate-and-state frictional fault properties.

Parameter	Symbol	Value
Direct-effect parameter	a	0.01-0.02
Evolution-effect parameter	b	0.014
Reference slip rate	V_0	10^{-6} m/s
Steady-state low-velocity friction coefficient at the slip rate V_0	f_0	0.6
Characteristic slip distance of the state evolution	L	0.2 m
Full weakened friction coefficient	f_w	0.1
Initial slip rate	V_{ini}	10^{-16} m/s
Weakened slip rate	V_w	0.1 m/s

Table S3: List of earthquakes used for back-projection calibration. Event information is taken from the Advanced National Seismic System (ANSS) Comprehensive Earthquake Catalog.

Time	**Latitude (°)**	**Longitude (°)**	**Depth (km)**	**Magnitude**
2019-07-12T13:11:38	35.638	-117.585	9.95	4.9
2019-07-07T05:38:15	35.768	-117.578	10.57	4.52
2019-07-06T08:32:58	35.639	-117.491	3.14	4.56
2019-07-06T04:13:07	35.587	-117.617	7.94	4.8
2019-07-06T04:07:05	35.555	-117.524	5.58	5.01
2019-07-06T03:29:29	35.704	-117.511	11.13	4.51
2019-07-06T03:25:28	35.860	-117.668	11.21	4.97
2019-07-06T03:23:51	35.800	-117.605	12.43	5.37
2019-07-06T03:19:53	35.770	-117.599	8.00	7.1
2019-07-06T03:16:32	35.725	-117.554	0.88	4.97
2019-07-05T11:07:53	35.760	-117.575	6.95	5.36
2019-07-04T18:56:06	35.716	-117.560	1.92	4.58
2019-07-04T18:39:44	35.601	-117.597	2.81	4.59
2019-07-04T17:33:49	35.705	-117.506	10.71	6.4

Table S4: Assumed hypocenter location from the QTM catalog (*1*).

Event	**Latitude (°)**	**Longitude (°)**	**Depth (km)**
Foreshock	35.70421	-117.49392	10.5
Mainshock	35.77623	-117.59286	8.0

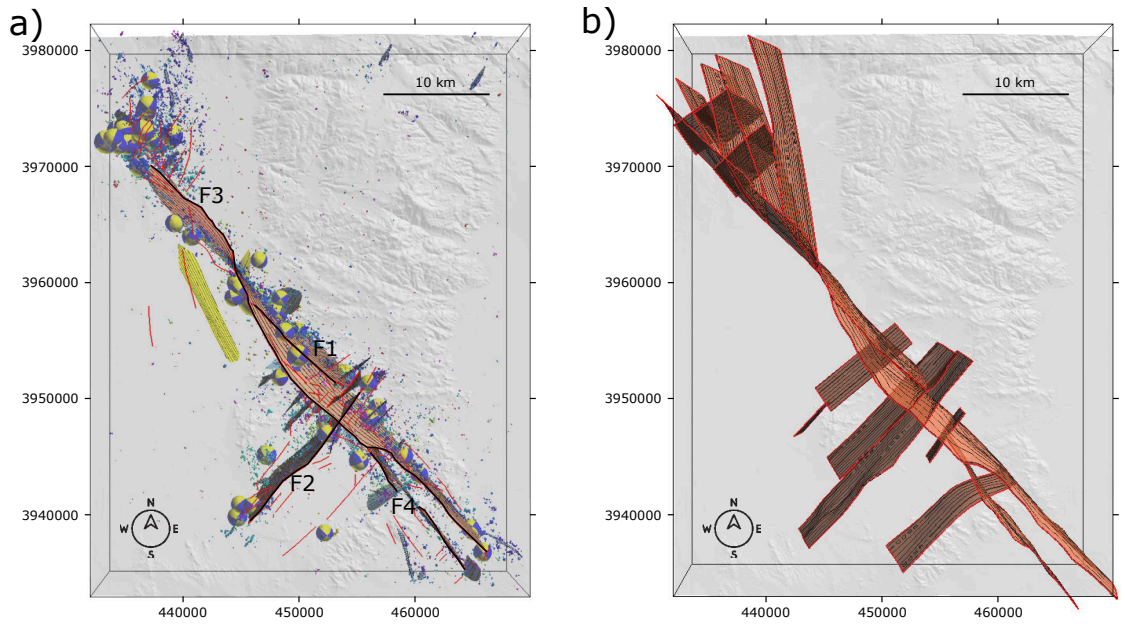

Figure S1: Top-view of (a) the constructed 3D fault network and (b) fault representations for the Ridgecrest earthquake sequence from the SCEC community fault model CFM, version 5.3 (*49*). Topography is overlain in transparent grey. In (a), focal mechanisms of aftershocks of magnitude larger than $M_{\mathrm{w}}4$ are represented as 3D spheres (*110*). When viewed from above, these are equivalent with the lower hemisphere stereographic projection representation typically plotted in tectonic maps. The three NW-SE trending right-lateral faults, F1, F3, and F4, and the conjugate NE-SW trending left-lateral fault, F2, are labeled.

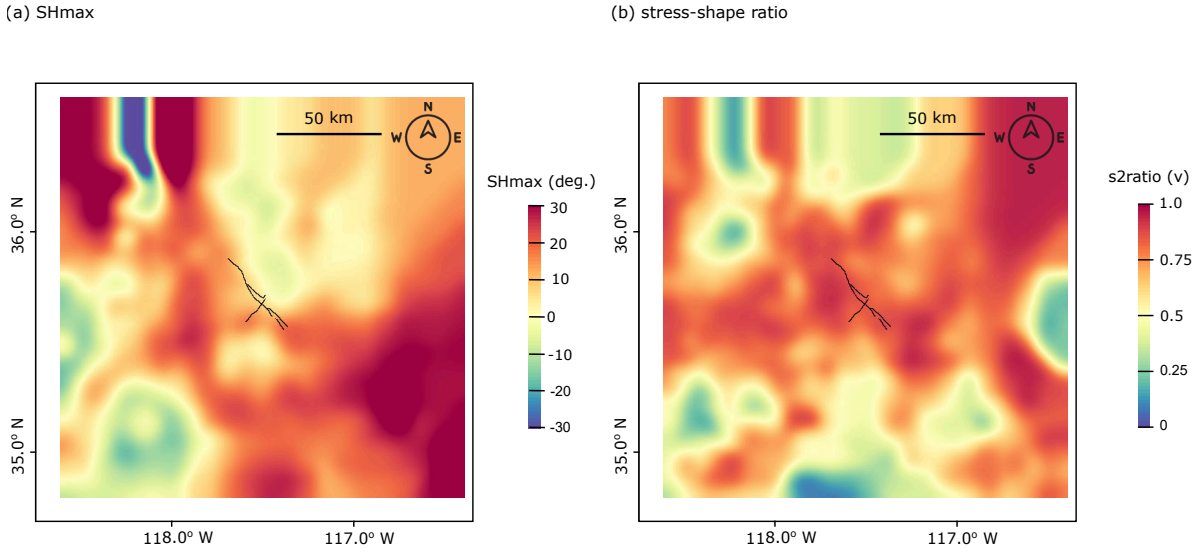

Figure S2: (a) SH_{max} and (b) stress-shape ratio ν computed from the YHSM-2013 dataset (*23*). Note that the data from YHSM-2013 are projected, and smoothed, as detailed in Methods Section .

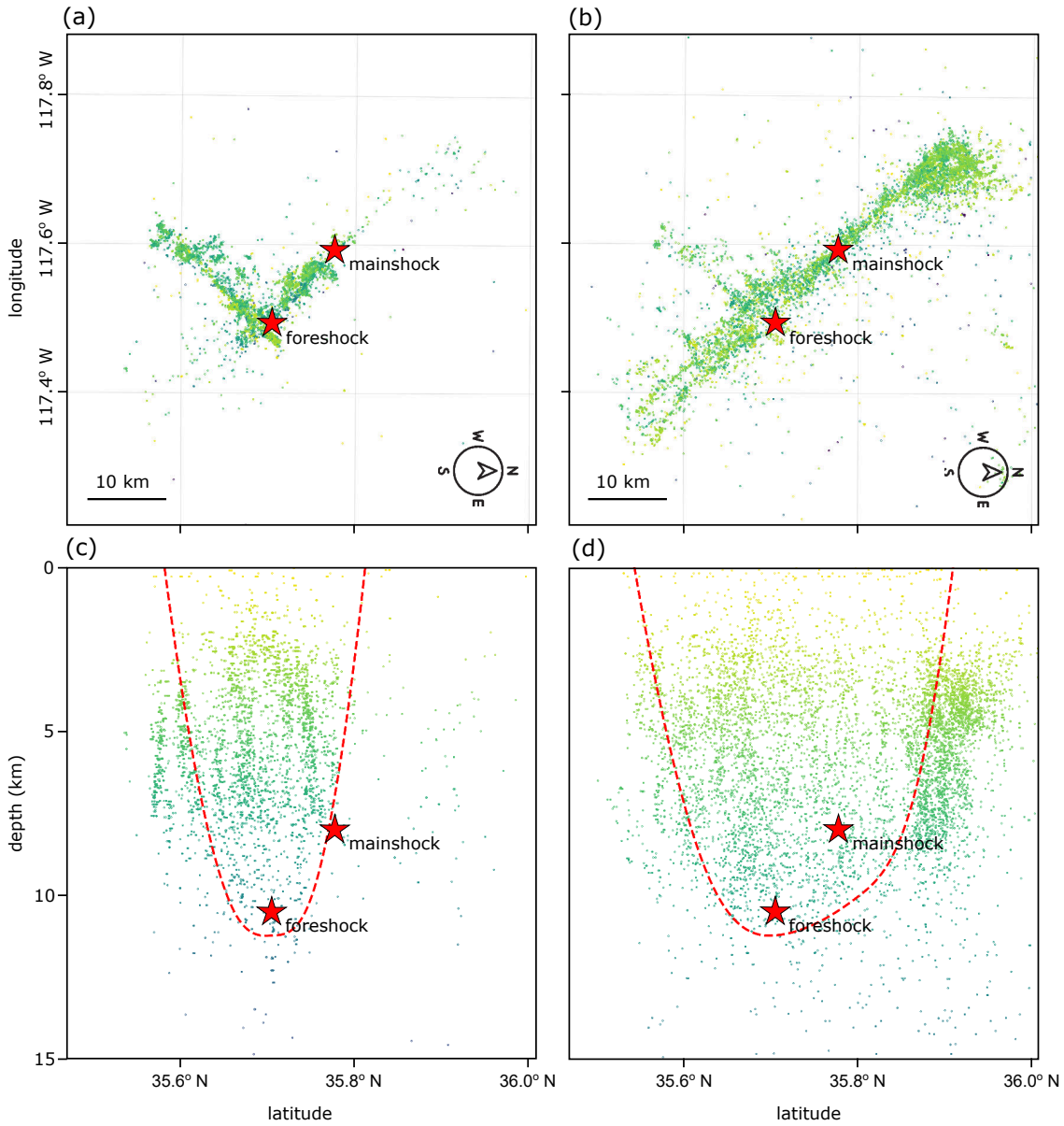

Figure S3: Assumed variations of seismogenic depth z_{seis} with latitude, constrained from aftershock locations (*1*). Deviatoric stresses smoothly tapper below z_{seis} (see Methods). Aftershock locations of (a) the foreshock and (b) the mainshock, using the same latitude x-axis as c) and d). Distribution of aftershocks with depth and latitude and assumed variation of z_{seis} (red dashed line) for (c) the foreshock and (d) the mainshock. The red stars are the hypocenter locations of both earthquakes.

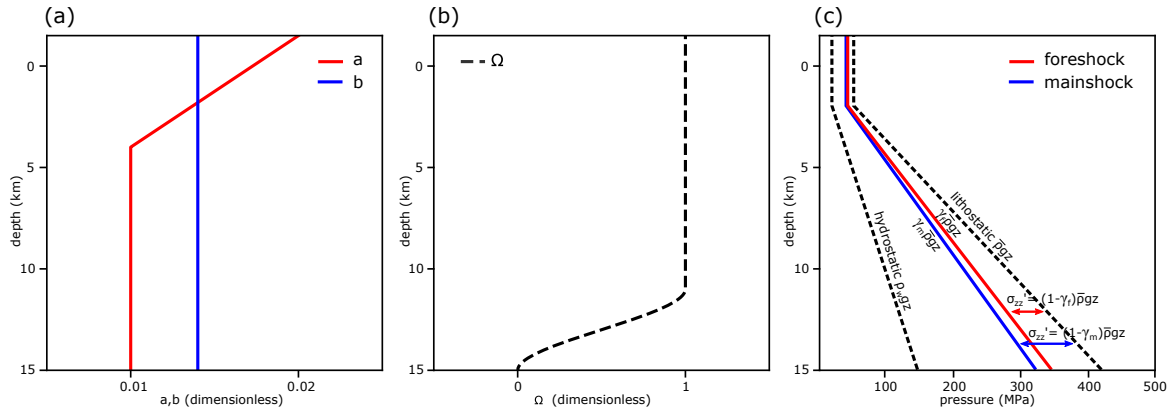

Figure S4: Depth-dependent friction and stress parameters. (a) a and b friction parameters. (b) Stress tapering function Ω. Ω tappers the deviatoric stresses below the seismogenic depth z_{seis} (see Methods). Ω is here exemplarily represented with z_{seis}=11 km. (c) The foreshock effective vertical stress $\sigma'_{\mathrm{zz}} = (1-\gamma_{\mathrm{f}})\bar{\rho}gz$ and the mainshock effective vertical stress $\sigma'_{\mathrm{zz}} = (1-\gamma_{\mathrm{m}})\bar{\rho}gz$, with $\gamma_f\bar{\rho}gz$ and $\gamma_m\bar{\rho}gz$ being the pore fluid pressures both below lithostatic pressure $\bar{\rho}gz$ but above hydrostatic pressure $\rho_{\mathrm{w}}gz$, with $\bar{\rho}$ as average density and ρ_{w} as water density. Pore fluid pressure ratio γ_{f} and γ_{m} are 0.83 and 0.77, respectively.

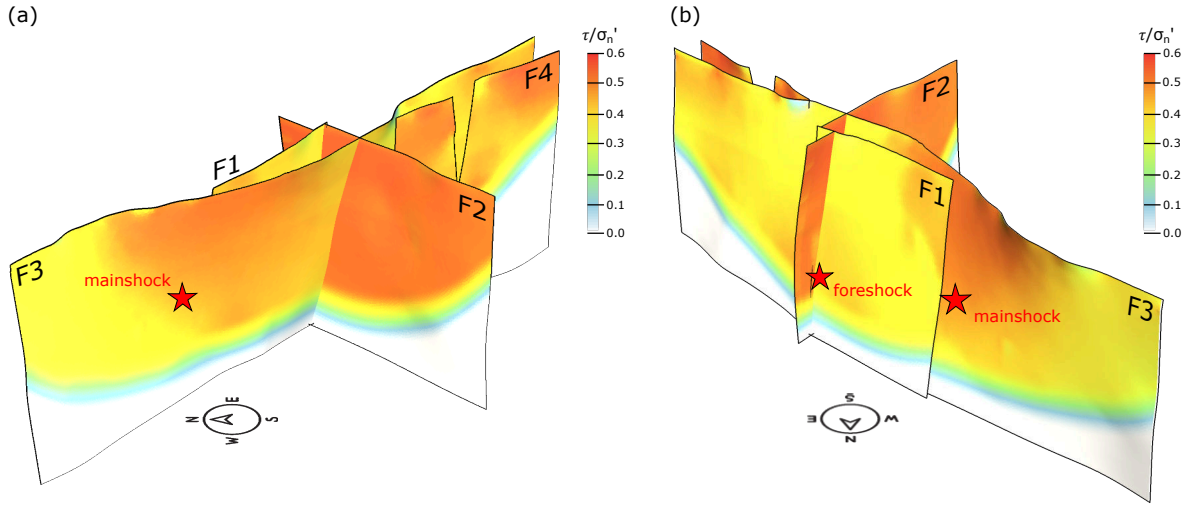

Figure S5: Ratio of initial shear stress τ over effective normal stress $\sigma_{\mathrm{n}}{}'$. (a) View from west and (b) from north.

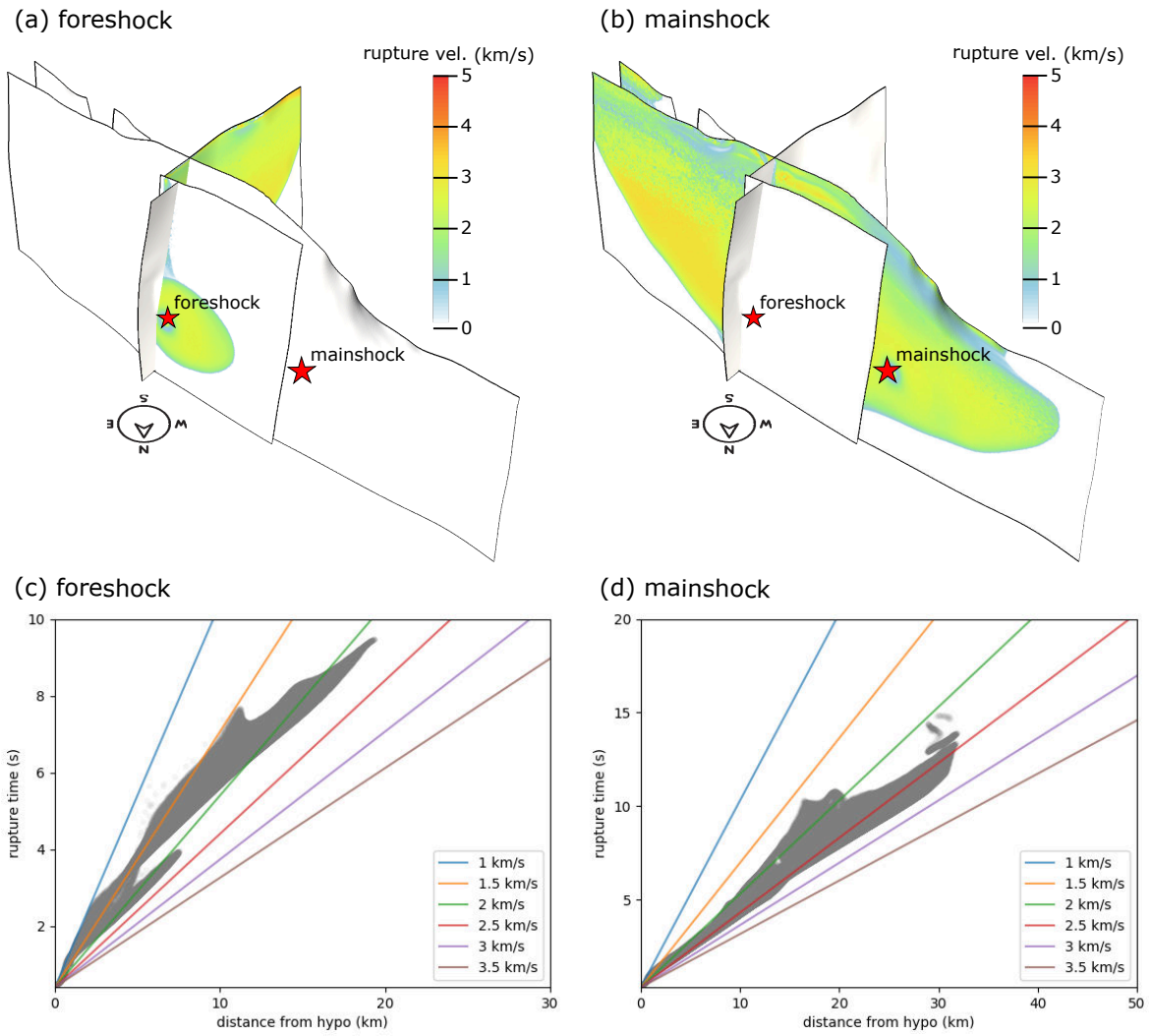

Figure S6: Rupture velocity distribution in the foreshock (a) and the mainshock (b) dynamic rupture scenarios. Distribution of rupture location relative to distance from (c) the foreshock and (d) the mainshock hypocenters with their rupture time (grey) across our complex fault system compared to constant rupture velocities (colored lines) We note that validation of dynamic rupture speed and moment release rate is challenged by the complexity of the dynamic rupture model. Also observational estimates may contain apparent slow initiation phases and lengthened slip duration, potentially due to secondary phase contamination and location uncertainties.

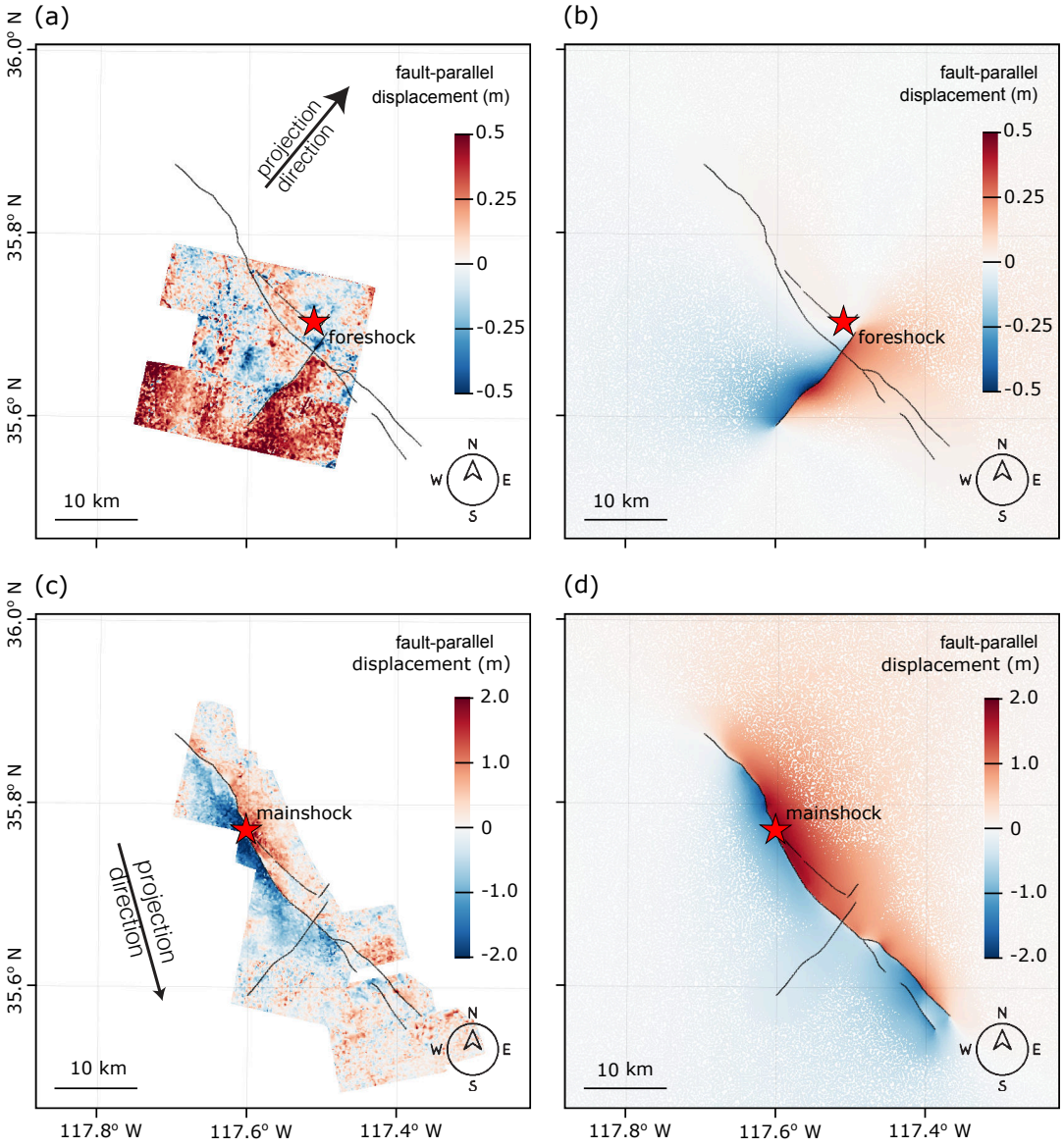

Figure S7: Comparison of the modeled and inferred surface displacements projected into fault parallel direction (with direction shown by arrow). Observations are from sub-pixel correlation of optical images from the PlanetScope imagery (*33*). (a) observation and (b) modeled surface displacements for the foreshock. (c) observation and (d) modeled surface displacements for the mainshock.

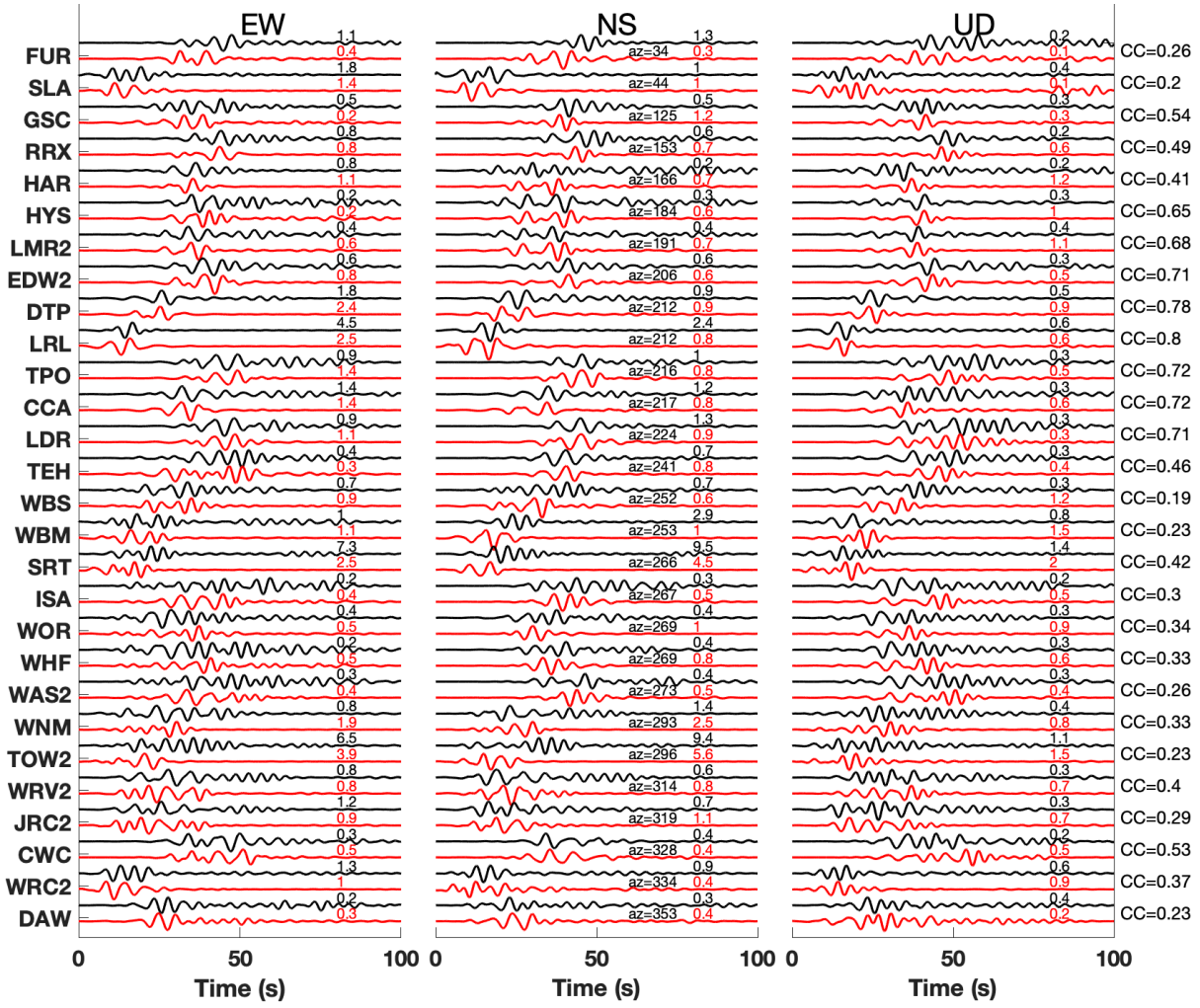

Figure S8: Comparison of modeled and observed ground motion time series for the Searles Valley foreshock. Synthetic (red) and observed (black) strong ground velocity at regional strong-motion stations shown in Figure 1, band-pass filtered between 0.1-0.3 Hz. CC are calculated from 300 s three-component waveforms. We normalize waveforms by their peak amplitudes (black numbers) to facilitate comparison and only consider unspoiled waveforms.

(a) foreshock teleseismic waveforms

(b) mainshock teleseismic waveforms

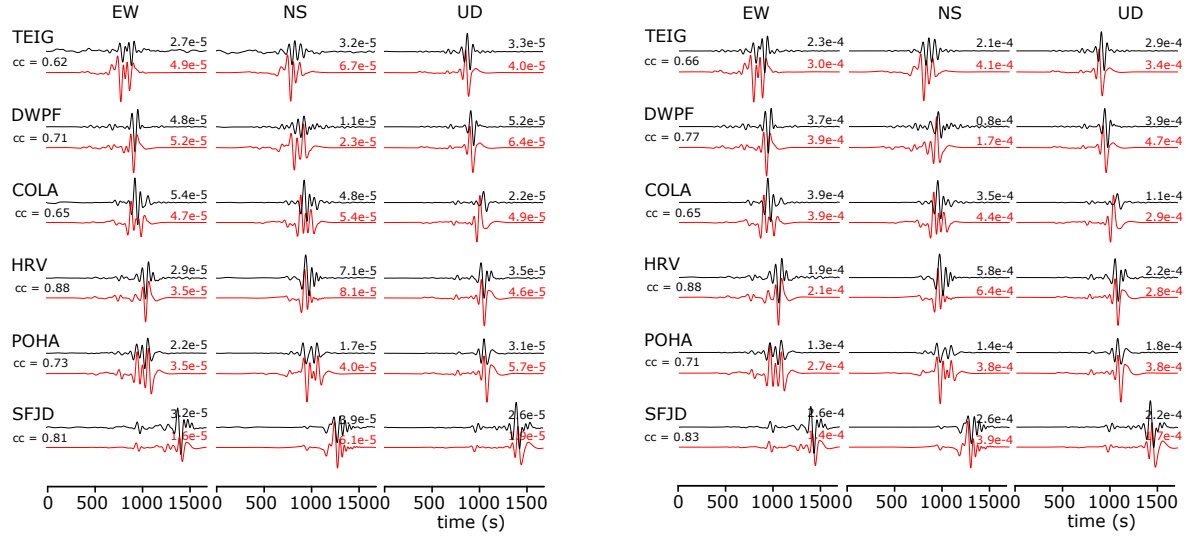

Figure S9: Comparison of synthetic (red) and observation (black) teleseismic waveforms at receiver locations shown in Figure 1a. A 0.002-0.02 Hz band-pass filter is applied. Synthetics are generated using Instaseis (*101*) and the PREM model including anisotropic effects, and accurate to a shortest period of 2 s (see Methods). At these 6 stations teleseismic observations for periods 50–500 s are matched across a wide azimuthal range with an average cross-correlation coefficient of ≈0.73.

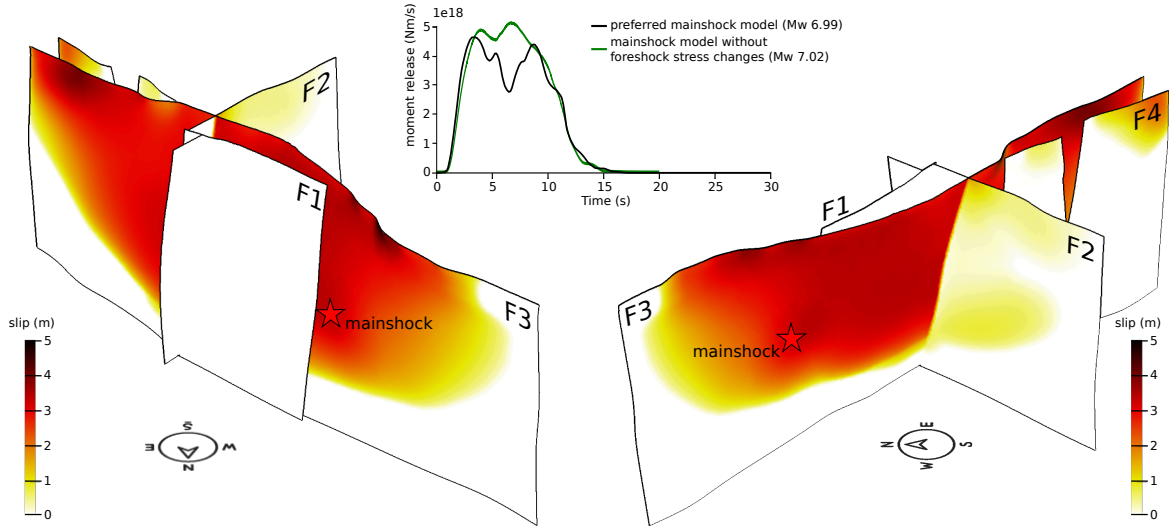

Figure S10: Alternative dynamic rupture scenario (i) of the mainshock which is not incorporating the foreshock dynamic and static stress changes. Final fault slip from two perspectives and moment rate compared to the preferred mainshock dynamic rupture scenario of Fig. S22. The reported moment magnitudes are calculated from slip on the faults, not accounting for the additional seismic moment due to off-fault deformation. See Video S3 for the evolution of absolute slip rate (m/s) across the fault network from 4 perspectives.

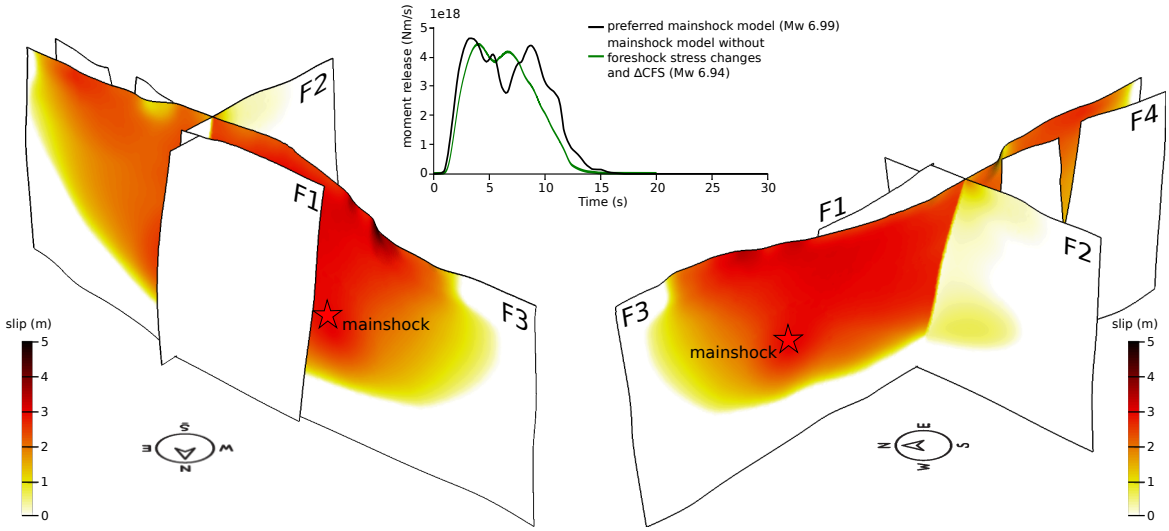

Figure S11: Alternative dynamic rupture scenario of the mainshock (ii) which is not incorporating the foreshock dynamic and static stress changes and in addition not incorporating the long-term ΔCFS. Final fault slip from two perspectives and moment rate compared to the preferred mainshock dynamic rupture scenario of Fig. S22. The reported moment magnitudes are calculated from slip on the faults, not accounting for the additional seismic moment due to off-fault deformation. See also Video S4 of the evolution of absolute slip rate (m/s) across the fault network from 4 perspectives.

(a) foreshock without long-term ΔCFS

(b) mainshock without long-term ΔCFS

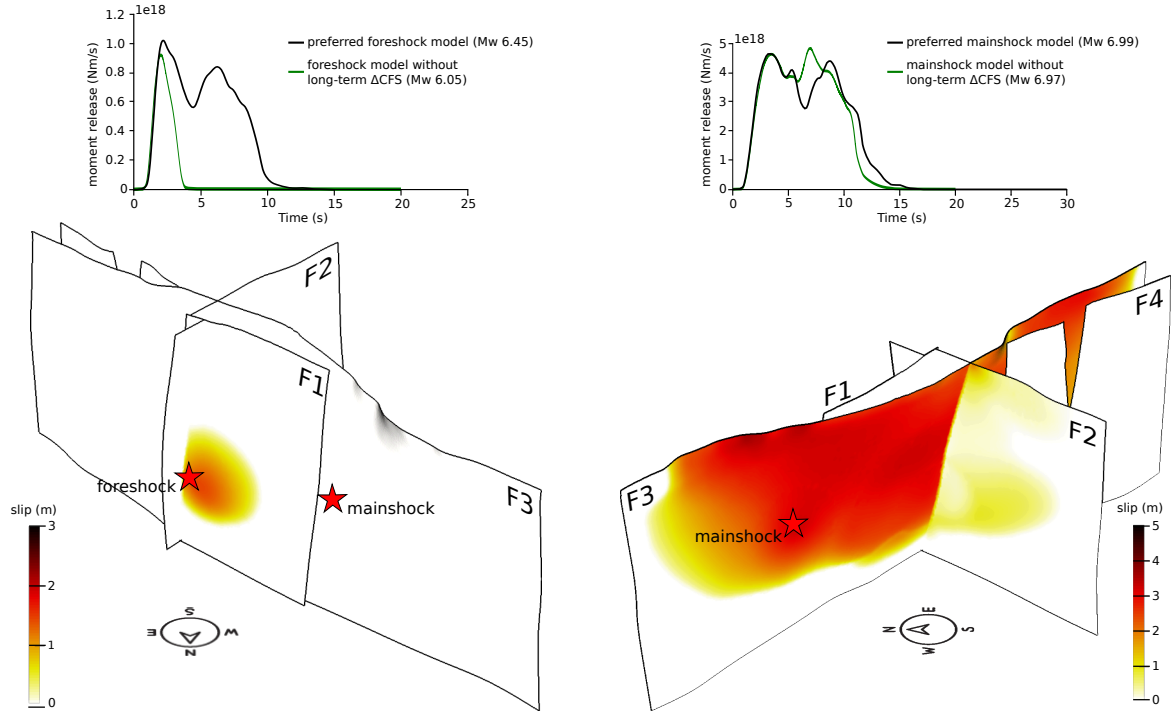

Figure S12: Alternative combined dynamic rupture models (iii) of foreshock and mainshock both not incorporating long-term ΔCFS. Final fault slip from two perspectives and moment rate compared to the preferred foreshock and mainshock dynamic rupture scenario of Fig. S22. The reported moment magnitudes are calculated from slip on the faults, not accounting for the additional seismic moment due to off-fault deformation. See Videos S5 and S6 for the evolution of absolute slip rate (m/s) across the fault network from 4 perspectives.

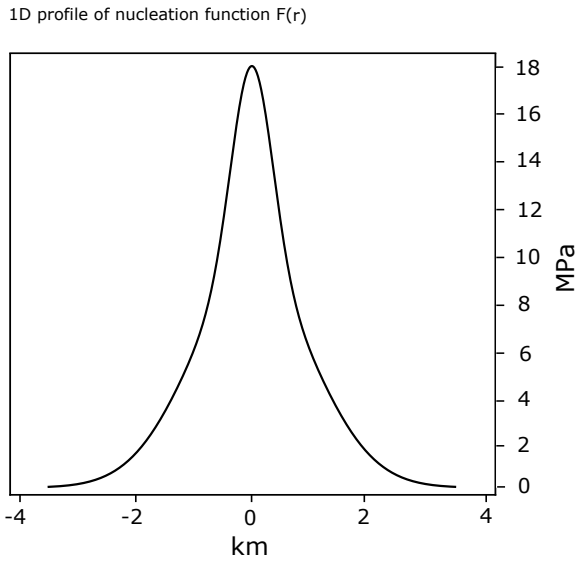

Figure S13: 1D profile of the dynamically required additional nucleation shear stress for the mainshock dynamic rupture scenario. The average nucleation stress is $\sim$3 MPa over the circular nucleation area of radius $r_{\rm nuc}$=3.5 km.

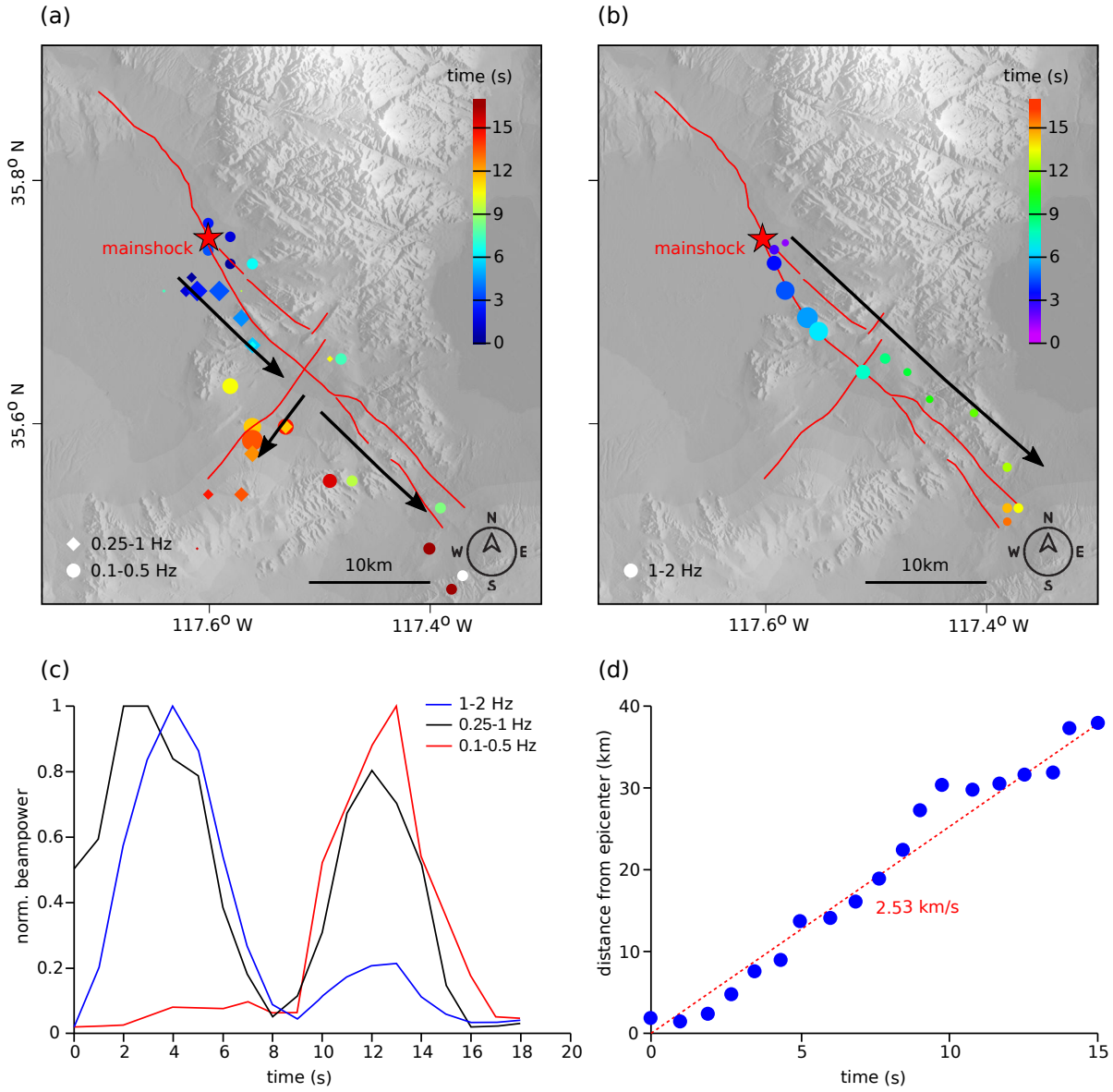

Figure S14: Frequency dependence of back-projection results (see Methods) when imaging the mainshock event. (a) High-frequency radiators imaged from data recorded by the Alaska array, in the frequency range 0.25–1 Hz and 0.1–0.5 Hz, mapped with diamonds and circles, respectively. (b) High-frequency radiators (circles) from data in the frequency range 1–2 Hz. The symbol sizes are proportional to the relative radiated energy and their colour represent the rupture time with respect to the event origin time. (c) Normalized beam-power for the three frequency bands represented in (a) and (b). (d) Projected location along the mainshock average trend N330 of high-frequency radiators for the frequency band 1–2 Hz versus time, suggesting a rupture speed of about 2.5 $\mathrm{km\,s^{-1}}$.

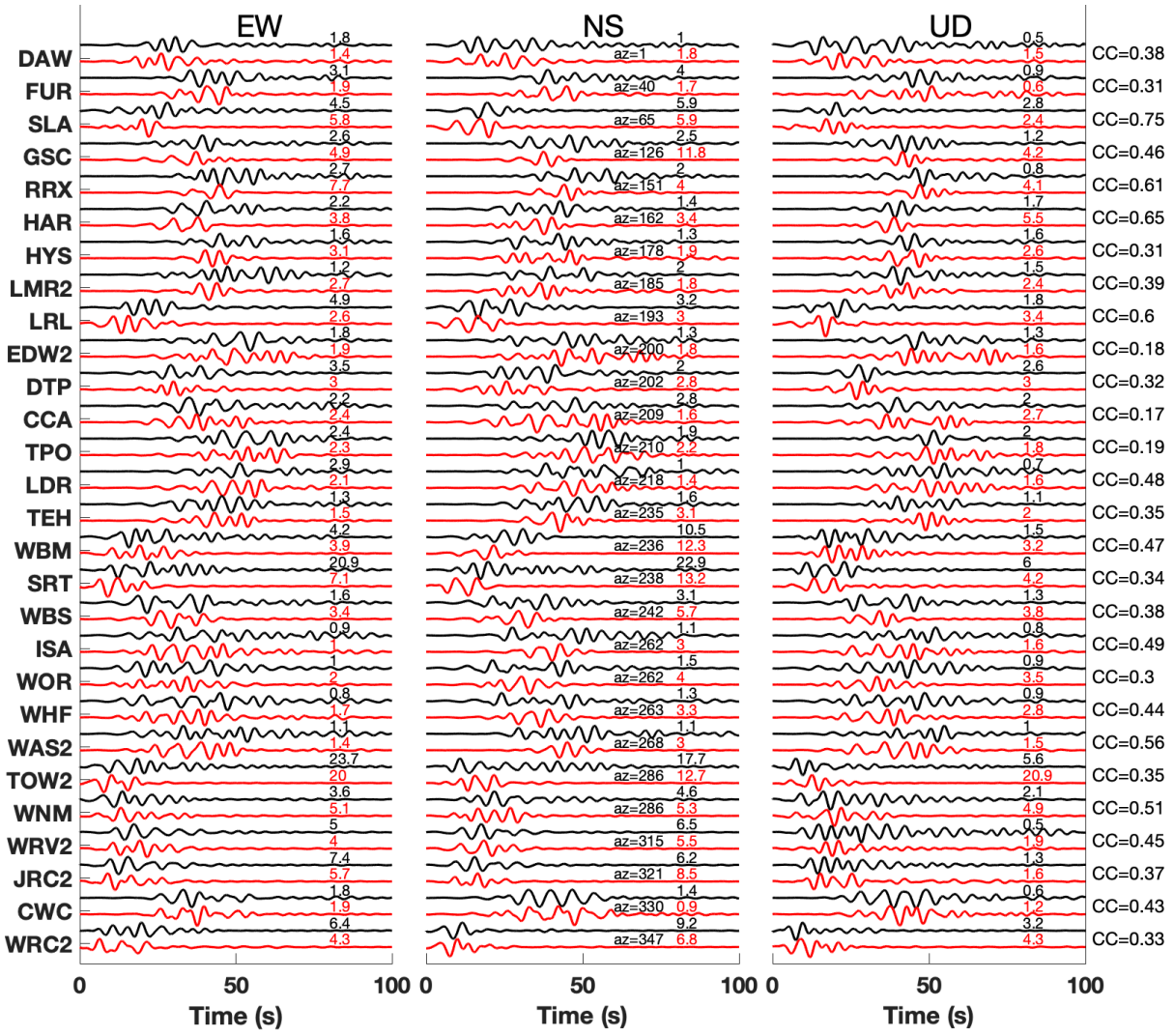

Figure S15: Comparison of modeled and observed strong ground motions for the Ridgcrest mainshock. Synthetic (red) and observed (black) ground velocity time series at regional strong-motion stations shown in Figure 1, band-pass filtered between 0.1-0.3 Hz. CC are calculated from 300 s three-component waveforms. We normalize waveforms by their peak amplitudes (black numbers) to facilitate comparison and only consider unspoiled waveforms.

(a) foreshock stress drop

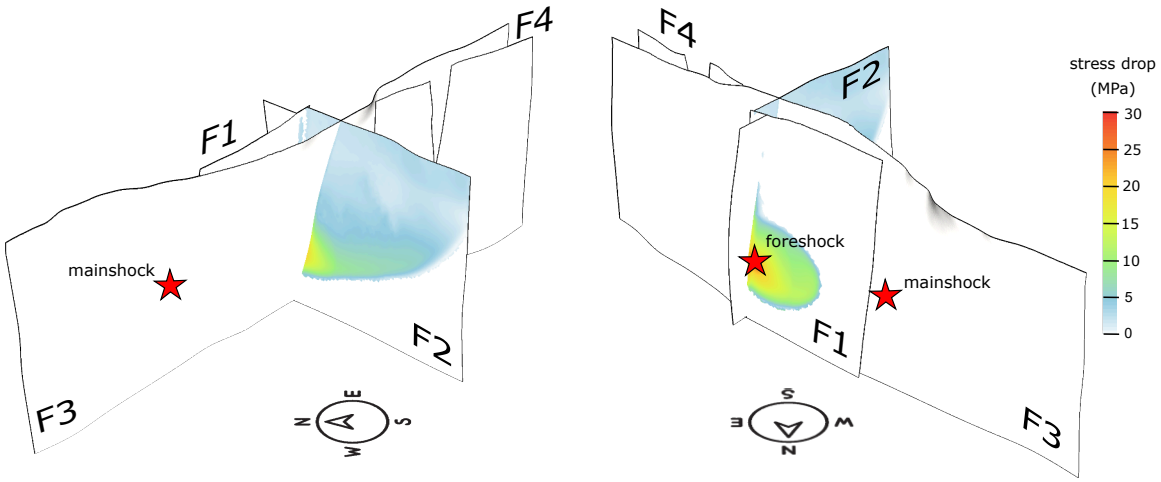

(b) mainshock stress drop

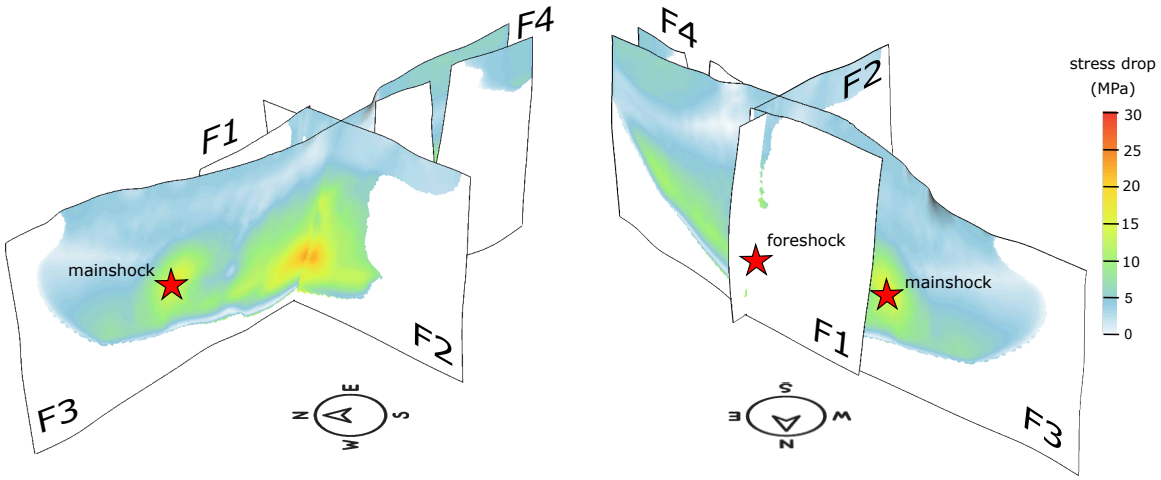

Figure S16: (a) Stress drop of the foreshock and (b) the mainshock dynamic rupture scenario. Left: view from west. Right: view from north.

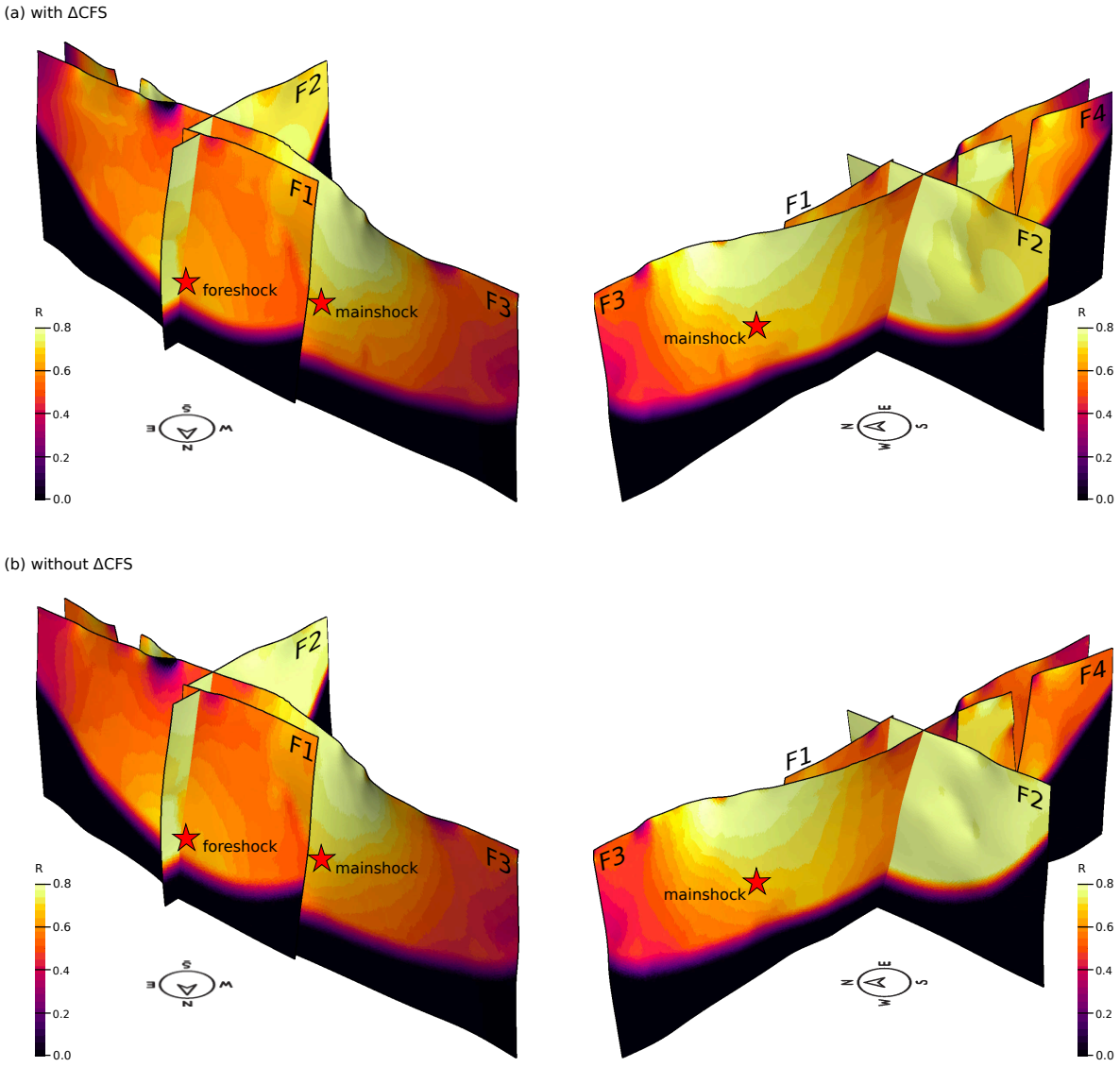

Figure S17: Relative prestress ratio R across the fault system for the preferred scenarios with long-term ΔCFS (left) and for alternative model (iii) without long-term ΔCFS (right). Mainshock and foreshock hypocenters are denoted by black stars.

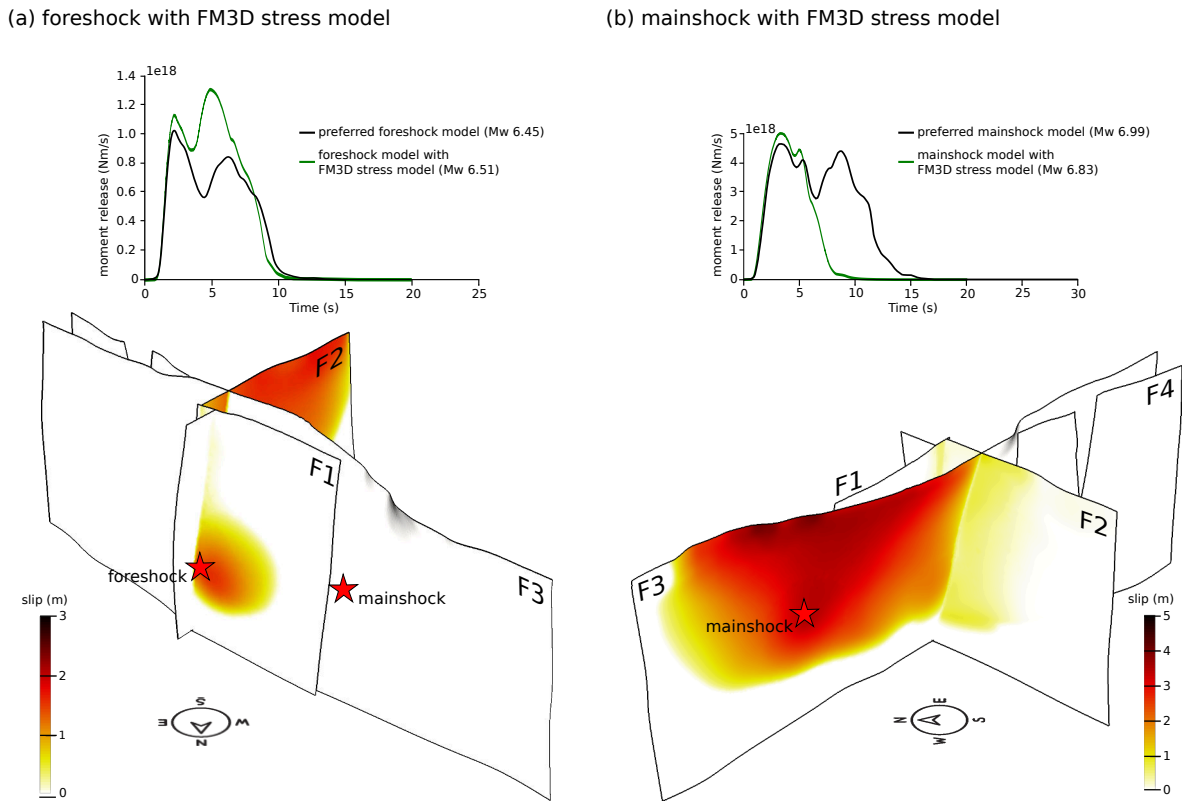

Figure S18: Alternative combined dynamic rupture models (iv) of foreshock (a) and mainshock (b), both incorporating the community stress model FM3D (*79*). Final fault slip and moment rate compared to the preferred foreshock and mainshock dynamic rupture scenarios, that adapt the community stress model YHSM-2013 (*23*) instead. The reported moment magnitudes are calculated from slip on the faults, not accounting for the additional seismic moment due to off-fault deformation. See Videos S7 and S8 for the evolution of absolute slip rate (m/s) across the fault network from 4 perspectives.

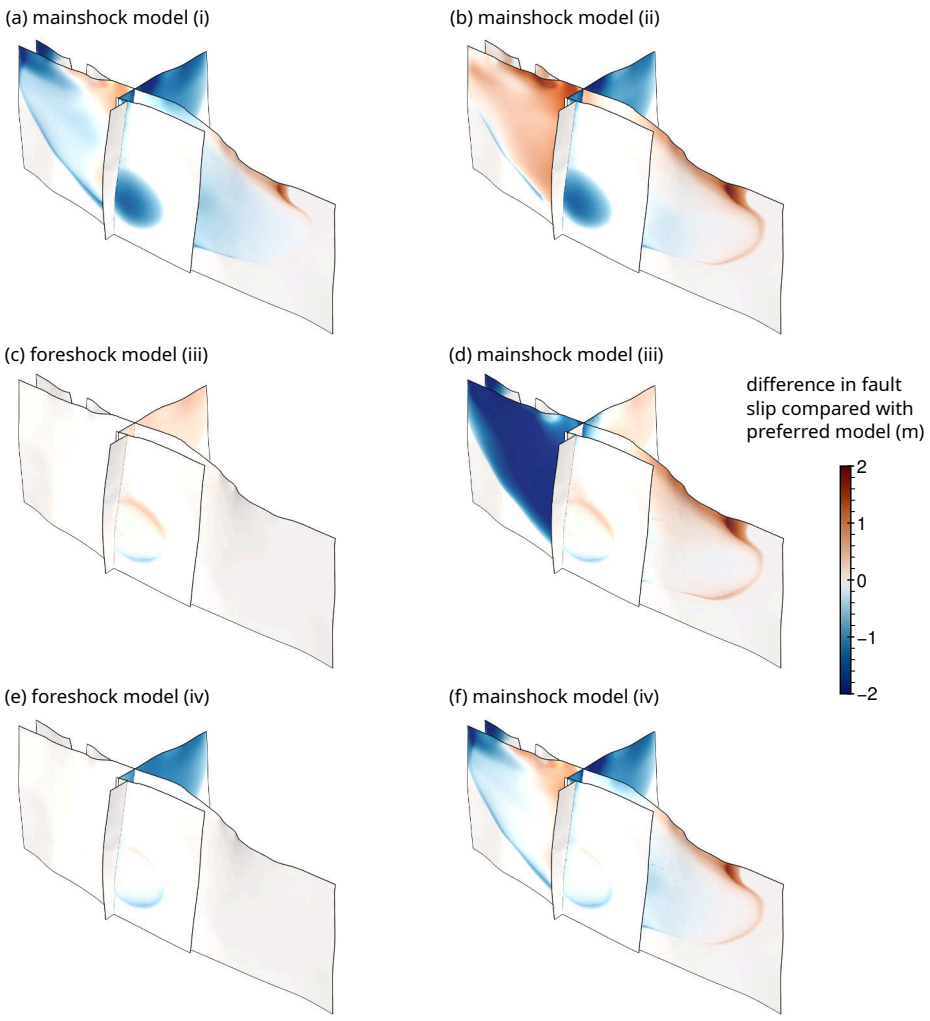

Figure S19: Difference in fault slip for models (i) to (iv) compared with preferred model in (m). Model (i) is not incorporating the foreshock stress changes. Model (ii) is not incorporating the foreshock stress changes and the long-term ΔCFS. Model (iii) is not incorporating the long-term ΔCFS. Model (iv) incorporates the community stress model FM3D (*79*).

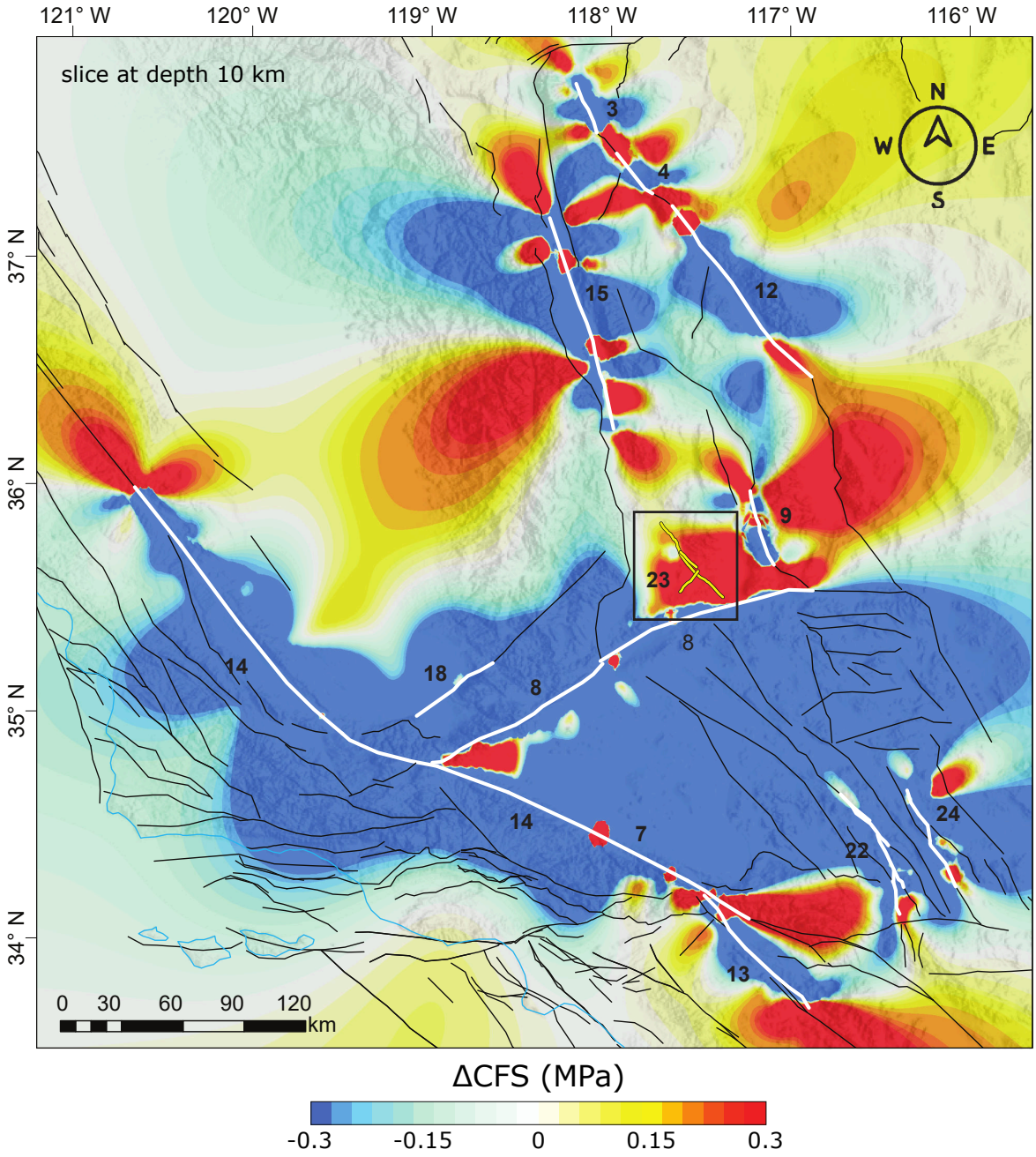

Figure S20: Pre-Ridgecrest cumulative Coulomb failure stress change (ΔCFS) from the events listed in Table S1, here plotted with white lines, at 10 km depth computed assuming a NW-striking fault plane of strike=318°, dip=88°, and rake=-170° and an effective friction coefficient f'=0.4, illustrating the 3D cumulative co- and post-seismic stress change model.

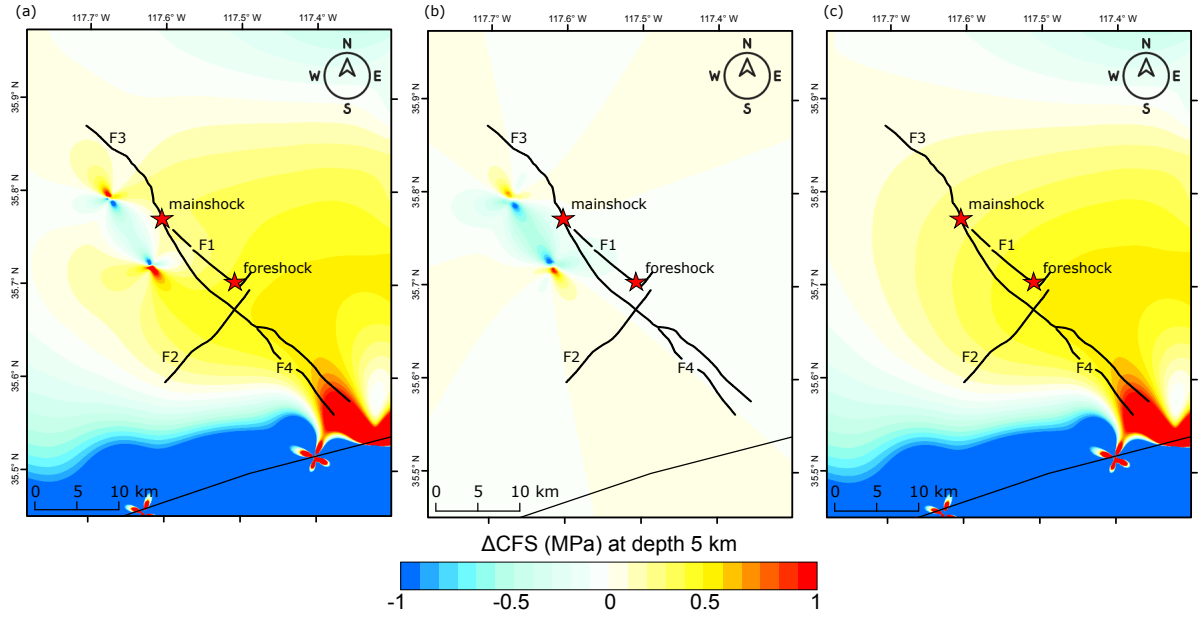

Figure S21: Pre-Ridgecrest cumulative Coulomb failure stress change (ΔCFS) isolating the effects of the two 1995 M_w 5.8 and M_w 4.9 earthquakes. (a) same as Figure 1b but with a smaller data range, ΔCFS of all events listed in Table S1 sliced at 5 km depth computed assuming a NW-striking fault plane of strike=318°, dip=88°, and rake=-170° and an effective friction coefficient f'=0.4. (b) ΔCFS of only the 1995 Ridgecrest M_w 5.8 and M_w 4.9 events. (c) ΔCFS of all events omitting the 1995 M_w 5.8 and M_w 4.9 events.

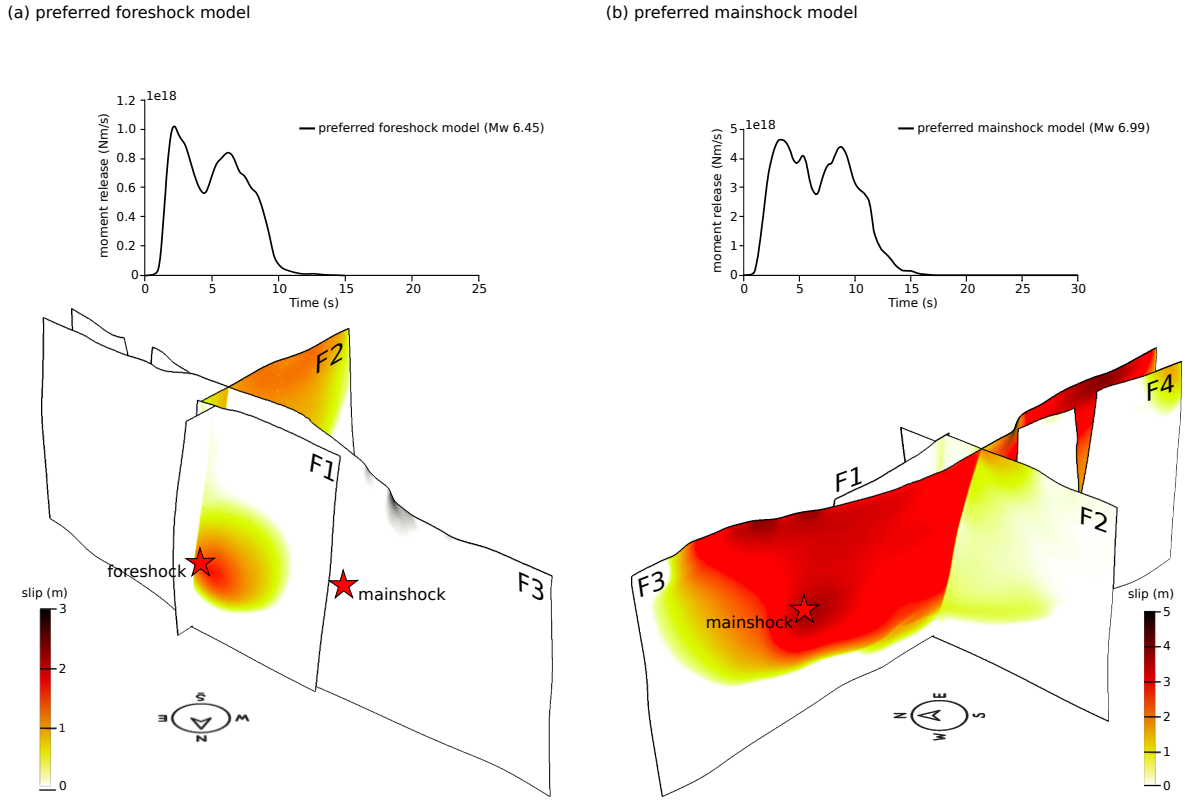

Figure S22: Preferred foreshock (a) and mainshock (b) dynamic rupture scenarios. Final fault slip from two perspectives and moment rate release.